Biotite supports long-range diffusive transport in dissolution-precipitation creep in halite

Berit Schwichtenberg[1], Florian Fusseis[1], Ian B. Butler[1], and Edward Andò[2]

[1]The University of Edinburgh, Edinburgh, United Kingdom
[2]Université des Alpes, Grenoble, France

Correspondence: Berit Schwichtenberg (berit.schwichtenberg@outlook.com)

Abstract. Phyllosilicates are generally regarded to have a reinforcing effect on chemical compaction by dissolution-precipitation creep (DPC) and thereby influence the evolution of hydraulic rock properties relevant to groundwater resources, geological repositories as well as fossil fuel reservoirs. We conducted oedometric compaction experiments on layered NaCl-biotite samples to test this assumption. In particular, we aim to analyse slow chemical compaction processes in the presence of biotite on the grain scale and determine the effects of chemical and mechanical feedbacks. We used time-resolved (4D) microtomographic data to capture the dynamic evolution of the transport properties in layered NaCl-NaCl/biotite samples over 1619 and 1932 hours of compaction. Percolation analysis in combination with advanced digital volume correlation techniques showed that biotite grains influence the dynamic evolution of porosity in the sample by promoting a reduction of porosity in their vicinity. However, the lack of preferential strain localisation around phyllosilicates and a homogeneous distribution of axial shortening across the sample suggests that the porosity reduction is not achieved by pore collapse but by the precipitation of NaCl sourced from outside the NaCl/biotite layer. Our observations invite a renewed discussion of the effect of phyllosilicates on DPC, with a particular emphasis on the length scales of the processes involved. We propose that, in our experiments, the diffusive transport processes invoked in classical theoretical models of DPC are superseded by chemo-mechanical feedbacks that arise on longer length scales. These feedbacks drive NaCl diffusion from the marginal pure NaCl layers into the central NaCl-biotite mixture over distances of several hundred μm and several grain diameters. Such a mechanism was first postulated by Merino et al. (1983).

1 Introduction

Chemically controlled compaction influences groundwater resources, geological waste repositories and CO_2 sequestration as well as fossil fuel reservoirs. One of the major processes involved in chemical compaction in the Earth's upper crust is dissolution-precipitation creep (DPC), a diagenetic and low-grade metamorphic deformation process that significantly contributes to cementation and reduction of porosity in sedimentary rocks (Rutter, 1983; Green, 1984; Tada and Siever, 1989; Gratier et al., 2013). Due to its impact on the diagenetic evolution of sediments it is crucial to study how DPC contributes to the dynamic change of petrophysical rock properties during compaction.

DPC describes a sequential chemo-mechanical process in a non-equilibrium system consisting of a solid phase and its
25 associated fluid under non-hydrostatic pressure conditions (Rutter, 1983; Gratier et al., 2013). The three successive steps in the
sequence are i) dissolution of material at stressed grain contacts, ii) diffusive mass transport through an intergranular fluid and
iii) local reprecipitation of dissolved material at low-stress sites (e.g. open pores, veins) (Rutter, 1983; Tada and Siever, 1989;
Gratier et al., 2013).

Phyllosilicates have been recognised to have a reinforcing effect on the dissolution process (e.g. Heald, 1956; Weyl, 1959;
30 Gratier, 1987) and act as loci for enhanced DPC. Whether this is due to enhanced reaction kinetics or effective transport
pathways, is still under debate (Gratier, 1987). Macente et al. (2018) explored this effect using time-resolved x-ray micro-
tomography to document chemical compaction in NaCl-biotite mixtures. They found that the increased porosity loss in the
biotite-bearing layer did not lead to an increased strain localisation. These observations pointed towards infilling of porosity
with material sourced outside the biotite-bearing layer rather than pore collapse, suggesting long-scale diffusive transport of
35 dissolved NaCl.

Reviewing diffusive transport during DPC shows that in theory four pathways for material transport need to be considered.
On the one hand intragranular Nabarro-Herring (Herring, 1950) and Coble creep (Coble, 1963), and on the other hand dif-
fusion through a free fluid either within grain boundaries or the open pore space (Durney, 1976; McClay, 1977). While the
intragranular diffusion mechanisms are activated at elevated temperatures (Raj, 1982), it is commonly accepted that diffusive
40 transport during low-temperature DPC occurs through an intergranular fluid film along grain boundaries (e.g. Raj, 1982; Rut-
ter, 1983; Gratier, 1987). Herein, transport distances do not exceed the grain size and dissolution sites are locally connected to
precipitation sites (Raj, 1982; Gratier, 1987; Groshong Jr, 1988; Gratier et al., 2013; Croize et al., 2013). However, theoretical
approaches (Durney, 1972, 1976; Merino et al., 1983; Lehner, 1995; Gundersen et al., 2002) as well as field evidence (Mimran,
1977; Buxton and Sibley, 1981) challenge this interpretation and suggest that long distance diffusive transport in the open pore
45 space needs to be considered as well.

Very few experimental data document the transport length scales of DPC. In this contribution we build upon the work
of Macente et al. (2018), and report the outcomes of further experiments on analogue samples of NaCl, using an improved
experimental set up and advanced analysis protocols for our time-resolved x-ray microtomography data. Our aim was to
determine length scales of diffusive transport in a dynamically evolving porosity during DPC.

2 Materials and Methods

2.1 Introduction

Aggregates containing sodium chloride (NaCl) and biotite were used to analyse the effect of DPC in granular materials.
As previous studies have shown (e.g. Peach, 1991; Bons and Urai, 1994; Peach and Spiers, 1996; Macente, 2017; Macente
et al., 2018), analogue materials are suitable to study deformation mechanisms at moderate P-T-conditions in experiments of
55 a tractable duration, and the results can be extrapolated to natural conditions. We chose NaCl as its solubility at low pressures
and temperatures is high compared to other constituent minerals of sedimentary rocks (Trurnit, 1968) and it has previously

been used for compaction experiments at room temperature (Spiers and Schutjens, 1990; Schutjens and Spiers, 1999; Renard et al., 2001, 2004; Gratier et al., 2013). It is further a material used in geological nuclear waste repositories (Powers et al., 1978), and its deformation behaviour is well-characterised.

2.2 Sample preparation

Two layered samples and one homogeneous sample were prepared for oedometric compaction experiments in low x-ray attenuation oedometer cells (Fig. 1) which are described in Macente (2017). The first sample (*SBS*) contained a central NaCl-biotite layer and two adjoining layers of pure NaCl as well as two layers of glass beads. The latter maintain permeability at the sample ends. For the second sample (*SB*) we increased the ratio of the NaCl-biotite layer and removed the top NaCl layer. A third pure NaCl sample (*S1*) served as a reference.

Masses for all components were calculated to meet the dimensions of cylindrical samples with $5\,\mathrm{mm}$ diameter and a desired starting height of $8\,\mathrm{mm}$. For the unconsolidated samples an initial porosity of $\sim 40\%$ was assumed which was also included into the calculation. The absolute heights of the samples were determined after loading the oedometers with the granular aggregate. Analytical grade NaCl and natural biotite were chosen as main components for the samples, as the difference in the x-ray attenuation results in a sufficient contrast in the reconstructed μCT data. The granular NaCl was sieved to a grain size of 250-300 μm. Biotite of granodioritic origin (Lone Grove pluton, Texas, e.g. Zartman, 1964) was pre-processed by mineral separation techniques (conducted at GFZ Potsdam, who supplied the biotite mineral separate) and sieved to a grain size of 200-500 μm. Acid washed glass beads with a diameter of 212-300 μm were added as chemically inert and permeable top and base layers.

The individual sample components were introduced into the sample cell by wet loading. Saturated NaCl-brine was injected into the bottom of the sample cell. For the two biotite-bearing samples (*SBS & SB*) glass beads and NaCl were sequentially poured into the brine followed by a homogeneous slurry of NaCl and 20 wt% biotite. For the pure NaCl sample dry NaCl was poured into the injected brine. All samples were covered at the top and bottom with a disc of filter paper to prevent blockage of the fluid inlet and outlet.

After the piston was inserted into the oedometer, the samples were flushed with brine to saturate the entire pore space with fluid.

2.3 Experimental setup

The experimental setup was designed to run three oedometric compaction experiments simultaneously (Fig. 2). We adopted the basic setup from Macente et al. (2018) and added a thermally insulated environment, vibration damping, pressurised fluid pumps and chemically inert glass beads layers to gain better control of parameters and establish a better characterised system. Oedometer cells as described in Macente et al. (2018) were modified by sealing the sample cell with an o-ring around the piston in order to withstand fluid pressure of $0.5\,\mathrm{MPa}$. The latter was applied in two different ways. For the *SBS* sample we used *Cetoni neMESYS* syringe pumps feeding a fluid transfer vessel that isolated the metal-corrosive brine. The transfer vessel was composed of a silicone tube filled with saturated NaCl brine inside a pressure resistant glass column. Saturation of the brine
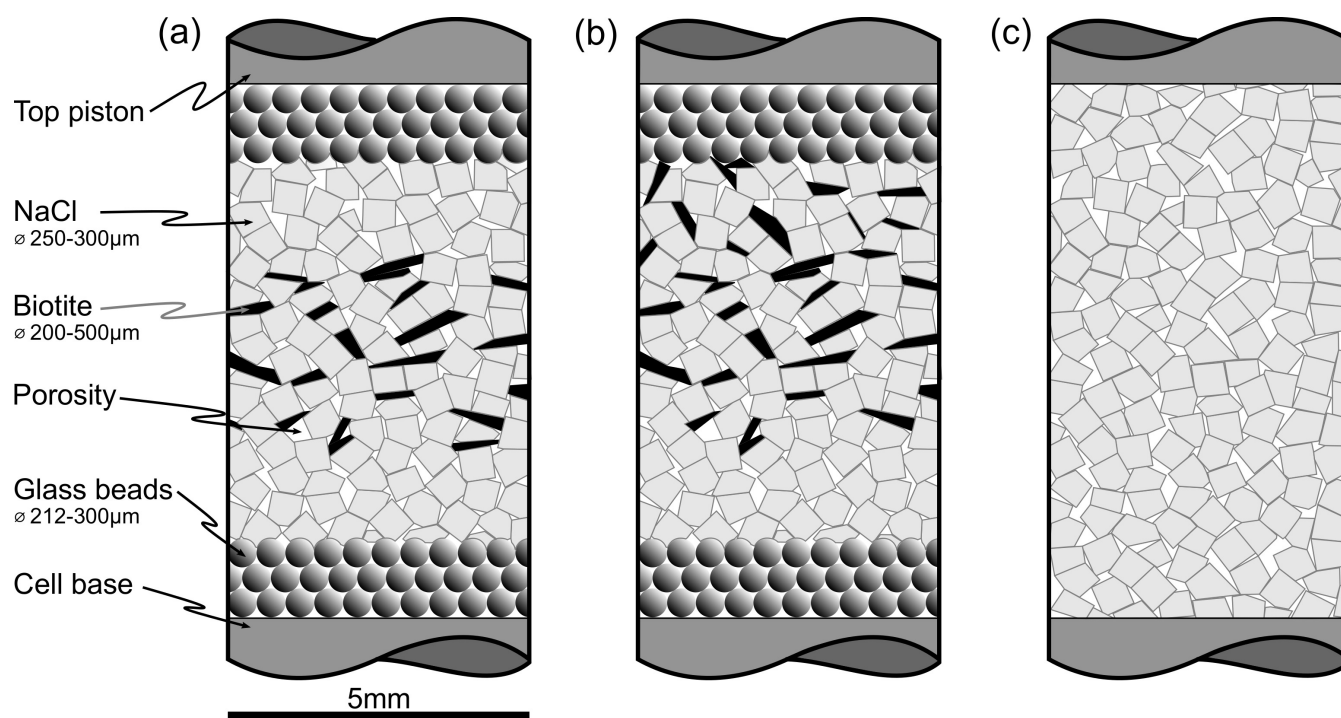
Figure 1. Schematic sketches of sample configurations of a) the NaCl-biotite-NaCl sample (*SBS*), b) the NaCl-biotite sample (*SB*) and c) the pure NaCl reference sample (*S1*) before deformation. Different shades of grey depict the single components but are not related to their appearance in the tomography scans. White angular patches represent the brine saturated pore space with arbitrary distribution of shape and size, light grey angular to square objects are cubic grains of analytical grade NaCl with a sieved grain size of 250-300 μm and black elongated angular shapes are biotite grains of 200-500 μm size. At the top and bottom of sample a) and b) dark grey circles describe acid washed glass beads of 212-300 μm diameter, which were inserted as chemically inert layer. The original samples have a diameter of 5 mm, note that the sketches are not to scale.

90   was guaranteed by the presence of solid NaCl in the reservoir. For the pure NaCl and the *SB* sample we used a plastic syringe that contained the corrosive brine itself and was driven by a pneumatic actuator. The experimental setup allowed maintaining a moderate pore fluid pressure to suppress gas bubbles while suppressing fluid advection.

The axial load was also applied by gas pressure driven pneumatic actuators when the oedometer cells were placed in loading frames following the construction of Macente (2017).

95   The experiments were run inside a thermally insulated box where the temperature was logged and found to be stable within $\pm 1.7\,°C$ over the course of the experiments. For the acquisition of microtomographic data, the odoemeters were disconnected from the fluid and pneumatic capillaries and mounted into the microtomography scanner (see next section).
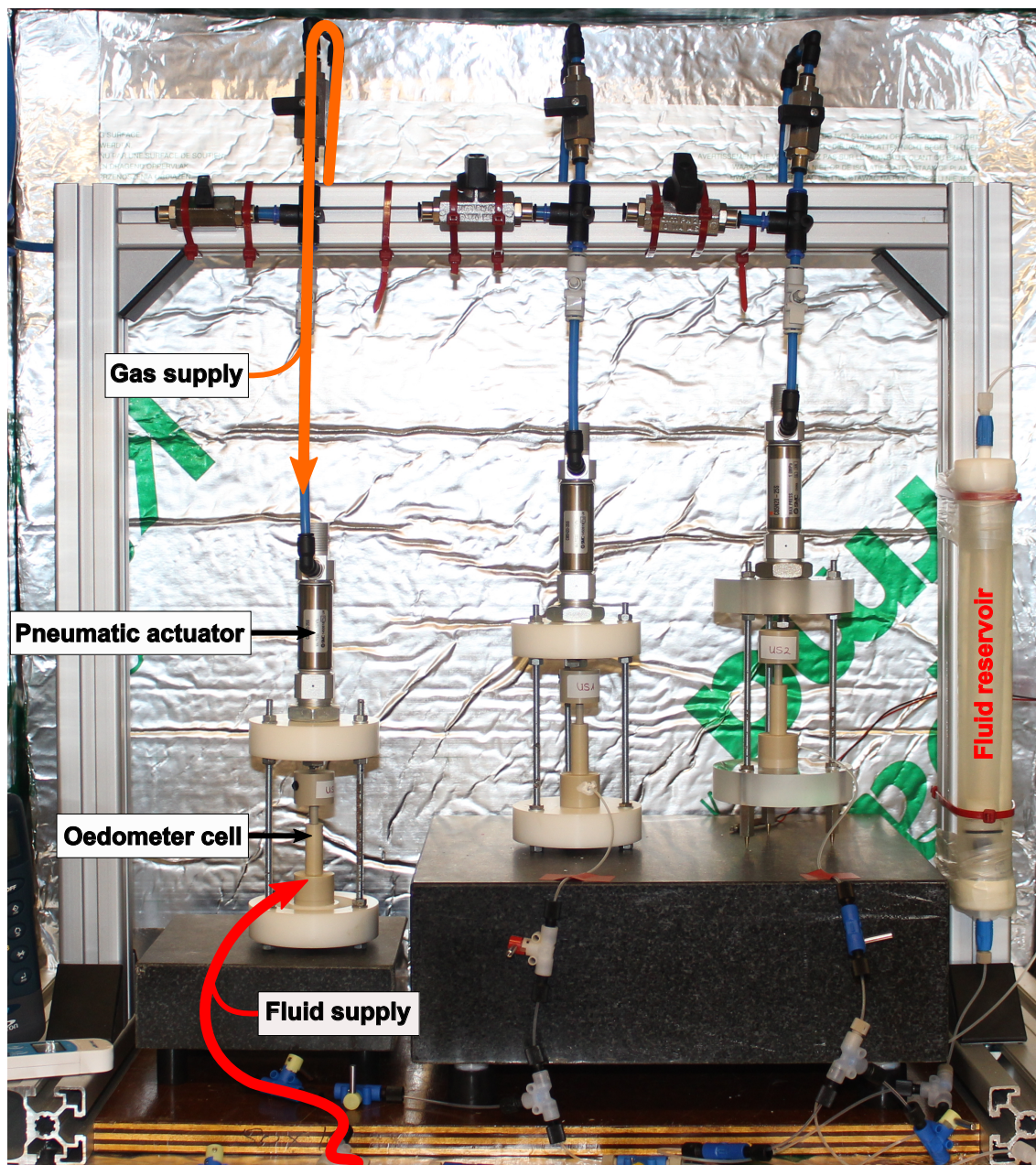
Figure 2. Experimental setup for oedometric compaction experiments. Three samples could be loaded simultaneously. Oedometer cells contained the cylindrical samples and were confined in straining frames during deformation. The load was applied by gas driven pneumatic actuators installed at the top of each frame. *Cetoni neMESYS* high-pressure syringe pumps were used to supply saturated NaCl brine via a fluid reservoir in order to maintain a pore fluid pressure sufficient to suppress gas bubbles in the samples. For the second experimental suit we replaced the fluid reservoir and high pressure pump with a brine filled syringe that was driven by another pneumatic actuator (not shown here). The oedometer cells were placed on acoustically dampened gabbro blocks to avoid external vibrations to reach the cells.

Upon initial loading, the unconsolidated granular samples were held at a constant effective load of 6.64 MPa and 10.5 MPa for samples *SBS* and *SB + S1* respectively for 60 minutes. After an initial compaction of 9 - 18% a reference scan was acquired

100 of the starting aggregate.

Following Macente (2017) and Macente et al. (2018), the same loading parameters were maintained throughout the experiment and consistently monitored over a total duration between 1089 and 1932 hours.

2.4 Data acquisition

During the experiment, the samples were scanned ex-situ on the x-ray microtomography instrument at the School of Geo-

105 sciences, University of Edinburgh in regular intervals (for acquisition parameters see Table A1, appendix). To enable this, the oedometers were unloaded and temporarily removed from the loading frames. Nineteen scans (*SBS* sample) and ten scans (*SB* sample) were acquired over a total duration of 1619 hours and 1932 hours, respectively. At the beginning scans were collected in shorter time intervals to image the rapidly progressing deformation within the first 200 hours of the experiment. As the compaction slowed down, the intervals between each scan were gradually extended to monitor chemical compaction processes. The

110 time-resolved 3D data series obtained in this way were then combined into three 4D data sets capturing the dynamic evolution of the porosity in the different samples.

2.5 Data processing

After each scan, *Octopus*® software v. 8.9 (Dierick et al., 2004) was used to reconstruct the μCT data from the radiographic projections. The resulting stack of 2D images, which contains a virtual representation of half of the sample, covers a volume

115 of $5 \times 10^3 \, \mu m^3$. Each time step comprises two scans, vertically translated to cover the entire sample including the sample base and the top piston. Reconstructed image stacks were merged using the image processing software *AVIZO*® v. 9.2. The relative shortening of the sample was calculated using

$$\varepsilon_t = \frac{L_0 - L_t}{L_0} \quad (1)$$

120 with the relative vertical shortening ε_t at the time t, the initial sample height L_0 and the sample height L_t at the time t. The height of each sample was determined from the merged microCT scans. The μCT data were prepared for analysis by pre-processing in *Fiji-ImageJ* (Schindelin et al., 2012). An uneven background of the reconstructed images was adjusted using the background correction plugin *BaSiC* (Peng et al., 2017) with the regularisation parameter $\lambda_D = 0.69$ and $\lambda_F = 1.71$ for the estimated dark-field and flat-field images, respectively. Denoising of the data was conducted by removing bright outliers

125 (threshold of 50) of 1.5 px and using the Non-Local Means filter (Buades et al., 2011) with a standard deviation of $\sigma = 3$ and a smoothing factor of 1. Biotite grains and porosity were segmented as single classes from the images, applying the machine learning tool *Trainable Weka Segmentation* (Arganda-Carreras et al., 2017, classifier in supplementary material). The latter was also used to segment NaCl grains in the pure NaCl sample but not in the two biotite-bearing samples. Due to a lack of contrast between the grey scales of NaCl, glass beads and the rims of biotite grains it was not possible to use simple

6

130 segmentation techniques. Instead we applied the *Deep Learning Segmentation* of *Dragonfly* software, version 2020.2 (Object
Research Systems , ORS). The resulting binarized image stacks were used for image analysis to quantify the porosity evolution
and NaCl migration.

2.5.1 Porosity measurements

The evolving porosity was determined during compaction as 2-dimensional porosity which was measured along the direction
135 of the loading axis as the relative area of the 2-dimensional binarized images. The results were plotted as the porosity on the
abscissa and the number of slices along the loading axis on the ordinate (Fig.12). Errors for this analysis were determined using
the probability measured in *Trainable Weka Segmentation*. The absolute error of the porosity measurement was defined as the
difference between the number of pixels belonging to the porosity with a certainty of $\geq 90\%$ to the total number of porosity
pixels measured from the segmented data. The absolute error is given in percent as it refers to the porosity which itself is a
140 relative number.

2.5.2 NaCl redistribution measurements

In order to quantify the amount of NaCl migrating within the sample we used two different methods to isolate a pure NaCl
signal from the rest of the sample. The first method is similar to the measurement of the 2D porosity. For each slice along the
loading axis of a microtomography scan we segmented the NaCl in the grey scale image using *Trainable Weka Segmentation*
145 for the pure NaCl sample and the *Deep Learning Segmentation* of *Dragonfly* software for both biotite-bearing samples. From
the segmented data we measured the relative area of NaCl in the 2-dimensional image and calculated its proportion relative
to the cross section of the sample. The results were plotted as relative NaCl content on the abscissa and the number of slices
along the loading axis on the ordinate (Fig.13).

Our second approach towards quantifying NaCl redistribution in the sample was based on 3D volumetric measurements of
150 segmented NaCl. The volumes of NaCl, biotite and porosity are measured relative to a subvolume in the compacting biotite-
bearing layer. We selected the subvolumes at fixed locations within the biotite-bearing domains of both samples that mimic the
compaction of the respective layer. The upper and lower limits of the subvolume were defined by two prominent biotite grains
at the top and bottom of each biotite-bearing layer which were easy to identify with progressing compaction of the sample. The
base of the subvolume was chosen as a 500x500 px square, which is representative of the sample but excludes the contact area
155 of the sample to the cell. This approach allowed us to measure the evolution of the NaCl volume within the biotite-bearing layer
with progressing deformation, with biotite acting as an internal standard.. The results were plotted as NaCl volumes relative to
a decreasing subvolume in the compacting biotite-bearing layer (Fig.14).

2.6 Digital Volume Correlation

Digital Volume Correlation (DVC) was used to quantify deformation on the grain scale between pairs of consecutive μCT
160 data sets using the python packages *SPAM* (Stamati et al., 2020) and *TomoWarp2* (Tudisco et al., 2017). A grid of regularly

spaced measurement points was defined in the reference image. Each of these points is the centre point of a cubic correlation window. A corresponding cube in the deformed image was transformed with a homogeneous deformation function in order to minimise a sum-of-squared-differences error function. The correlation parameters were individually tuned for each data series and are documented in Table 1. The DVC analysis was completed by strain determination. A finite strain tensor U and its first two invariants – the volumetric strain (Eq.(3)) and the deviatoric strain (Eq.(4)), were calculated from the locally measured displacement component of the deformation function.

$$U = U_{isotropic} * U_{deviatoric} \tag{2}$$

$$U_{isotropic} = J^{1/3} * I \tag{3}$$

$$U_{deviatoric} = \frac{1}{J^{1/3}} * U \tag{4}$$

where $U_{isotropic}$ is the isotropic or volumetric strain, and $U_{deviatoric}$ the deviatoric strain. I is the identity matrix, J the determinant of the strain tensor and its exponent refers to the dimension of the problem which is 3-dimensional in this case.

The mean strain-rates were obtained by dividing the magnitude of the strain tensor by the time (in seconds) between two analysed data sets.

With label analysis, also implemented in *SPAM*, we determined the rotation and rearrangement of single biotite grains with progressing deformation based on labelled and binarized data sets. For each microtomography scan we segmented the biotite grains as described in Sect. 2.5 and applied a watershed algorithm to separate the grains into individual particles with an allocated label. Further, we calculated the eigenvalues and eigenvectors from each particle's moment of inertia, which is in the case of biotite directly related to the shape and orientation of the particle. The orientations are represented as maximum eigenvectors perpendicular to the basal planes of the grains and plotted as densities in Lambert projections with the vertical loading axis in the centre of the plot (Fig. 6).

3 Results

3.1 Bulk compaction behaviour

3.1.1 Vertical shortening

The bulk compaction of the samples was monitored as vertical shortening and compaction rate over a total duration of 1089 hrs, 1619 hrs and 1932 hrs, for the reference sample (*S1*), the *SBS* and the *SB* samples, respectively.

All three samples showed a non-linear decrease in height. The *SB* sample accommodated a total strain of $\sim 26\%$ over 1932 hrs of compaction. Initially the sample shortened by $\sim 11\%$ within the first 19 hrs of compaction, resulting in a steep gradient

Solid Earth
Discussions
Open Access
EGU

Table 1. Correlation parameters used to conduct Digital Volume Correlation for different data series. The correlation window size, usually used in DIC applications, corresponds to 1+2× the half window size given in the table. The threshold value is simply implemented to skip correlation windows placed outside the sample based on their mean grey value

DVC parameters	SBS	SB	S1
Correlation half window size	30	30	30
Measurement point spacing	15	15	15
Low grey level threshold	4000	5000	16000

190   of the compaction curve, while in the following interval between 19 and 236 hrs, the compaction rate gradually decreased and stabilised after 324 hrs, indicating steady state deformation (Fig. 3). The compaction rates of the *SBS* sample and the pure NaCl reference sample followed similar trends. The *SBS* sample accommodated a total vertical shortening of $\sim 25\%$ after 1619 hrs of which $\sim 9\%$ occurred within the first 16 hrs of deformation. This sample reached steady state deformation after about 280 hrs. As the compaction of the reference sample was stopped after 1089 hrs, the total shortening of this sample was with $\sim 17\%$,

195   lower than the total shortening of the biotite-bearing samples. At comparable compaction stages of 1060 hrs and 1020 hrs, for the *SB* and *SBS* sample respectively, the difference between the reference and the biotite-bearing samples was approximately $\sim 10\%$. It is notable that the final scans in all three experiments were acquired before the compaction ceased.

   Analysis of the bulk strain rates ($\dot{\epsilon}$) with progressing compaction support these findings. On a double logarithmic scale (Fig. 3b), strain rates for all three samples decreased approximately linearly and dropped in total by two orders of magnitude from

200   $\sim 10^{-6}$ s^{-1} to $\sim 10^{-8}$ s^{-1}. Within the first 200 hours of compaction the strain rates decreased by one order of magnitude. The steady state deformation interval was characterised by a constant strain rate gradient of $\sim -5 \times 10^{-11}$s^{-1}. Linear regressions for the three strain rates over time t have the form of

$$\dot{\epsilon} = t^{-1.26} * e^{-9.81} \tag{5}$$

$$\dot{\epsilon} = t^{-1.09} * e^{-10.80} \tag{6}$$

205   $$\dot{\epsilon} = t^{-1.01} * e^{-11.16} \tag{7}$$

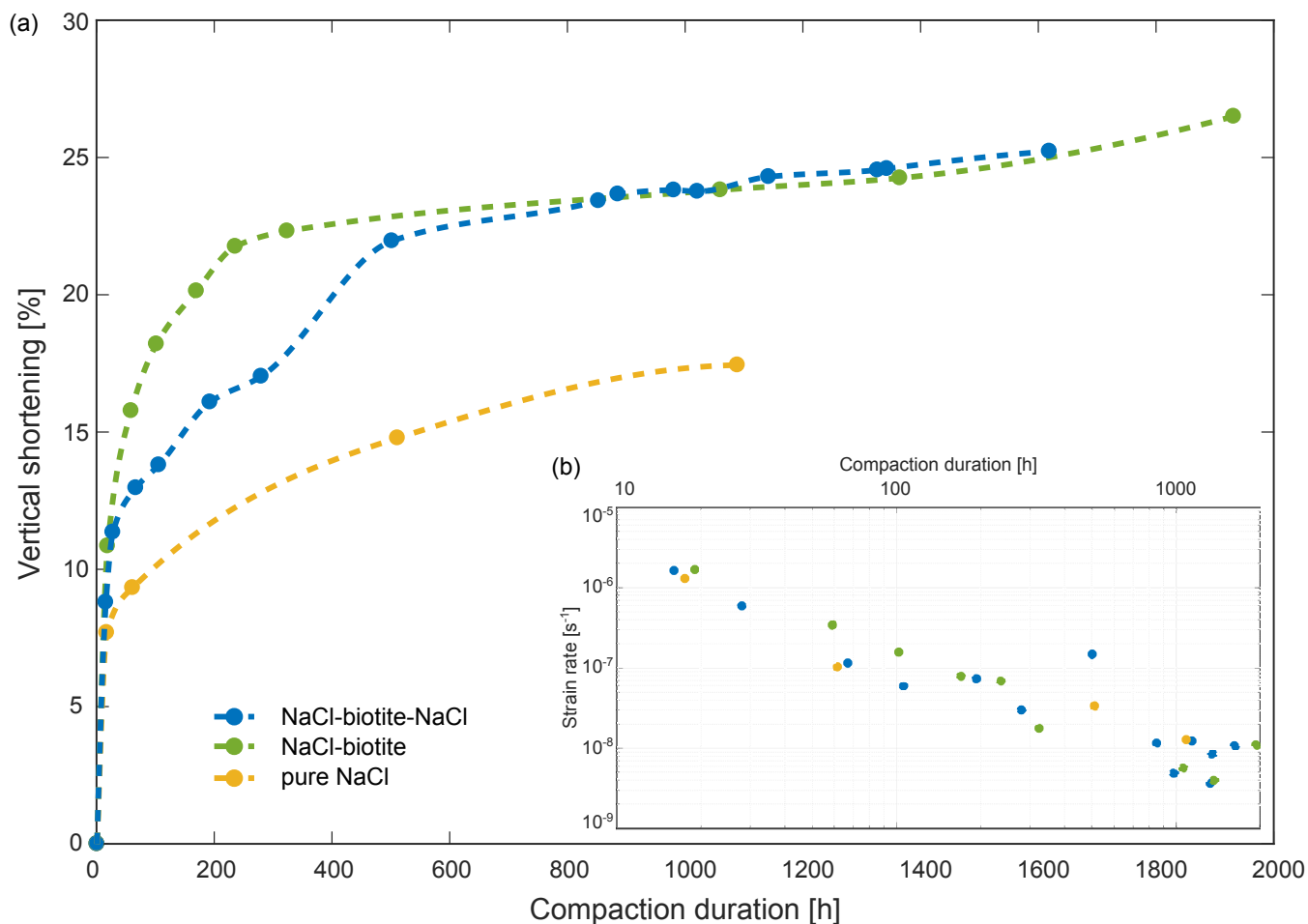for the *SB*, *SBS* and pure NaCl sample, respectively.

Figure 3. Bulk compaction curves (a) and strain rates (b) derived from μCT-data for three samples, *SBS* in blue, *SB* in green and pure NaCl in yellow. a) shows the vertical shortening of the samples with progressing deformation. We interpret the non-linearity of the curves as the transition from dominantly mechanical to chemical compaction. Note that all three samples show a similar trend with steady state deformation established after ~ 250 hours. In b) we plotted the corresponding bulk strain rates over the compaction duration.

3.1.2 Microstructures and compaction accommodation

Vertical slices through the geometrical centre of μCT data illustrate the evolution of the microstructure (Fig. 4). In the biotite-bearing samples porosity reduction, a change of the cubic habit of the NaCl grains and the establishment of flat interphase boundaries between NaCl and biotite grains can be observed over 100 and 60 hrs for *SBS* and the *SB* sample, respectively. Within the biotite-bearing layers, characteristic evidence for DPC (dissolution leading to grain indentation and re-precipitation of dissolved matter) was enhanced along phase boundaries (Fig. 4 a-h & 5). However, the pure NaCl layers as well as the NaCl reference sample showed, to a smaller extent, similar dissolution structures at later compaction stages. The efficiency of

the process becomes obvious on the grain scale (Fig. 5 and animation (S1) in supplementary material which shows a single

215 NaCl grain enclosed by two biotite grains with progressing deformation). We found that the orientation of the enclosing biotite

grains did not change significantly as the volume of the NaCl grain was reduced. We calculated the shortening of the single

NaCl grain to be $\sim 26\%$, which is similar to the shortening calculated for the bulk biotite-bearing sample (see Sect. 3.1.1).

The orientation of the maximum eigenvector of individual biotite grains was plotted in Lambert projections (Fig. 6). For both

biotite-bearing samples, areas with a high density of data points were located close to the centre of the plots, revealing that the

220 maximum eigenvectors of single biotite grains were orientated vertically and did not significantly rotate away from the vertical

loading axis after an instantaneous mechanical rearrangement of the grains.

Our analysis showed that the compaction was accommodated throughout the samples, independent of their composition.

Figure 7 shows the vertical displacement rate of the biotite-bearing layer and the bulk sample for different increments of

progressing deformation for the two biotite-bearing samples. The time intervals which correspond to the individual increments

225 are listed in the table below. At the beginning of the experiment the rate of both bulk samples was elevated compared to the

biotite-bearing layers. However, as compaction approached a steady state, the vertical displacement rates of the biotite-bearing

layer and the bulk sample became comparable and both asymptotically approached a value of zero.
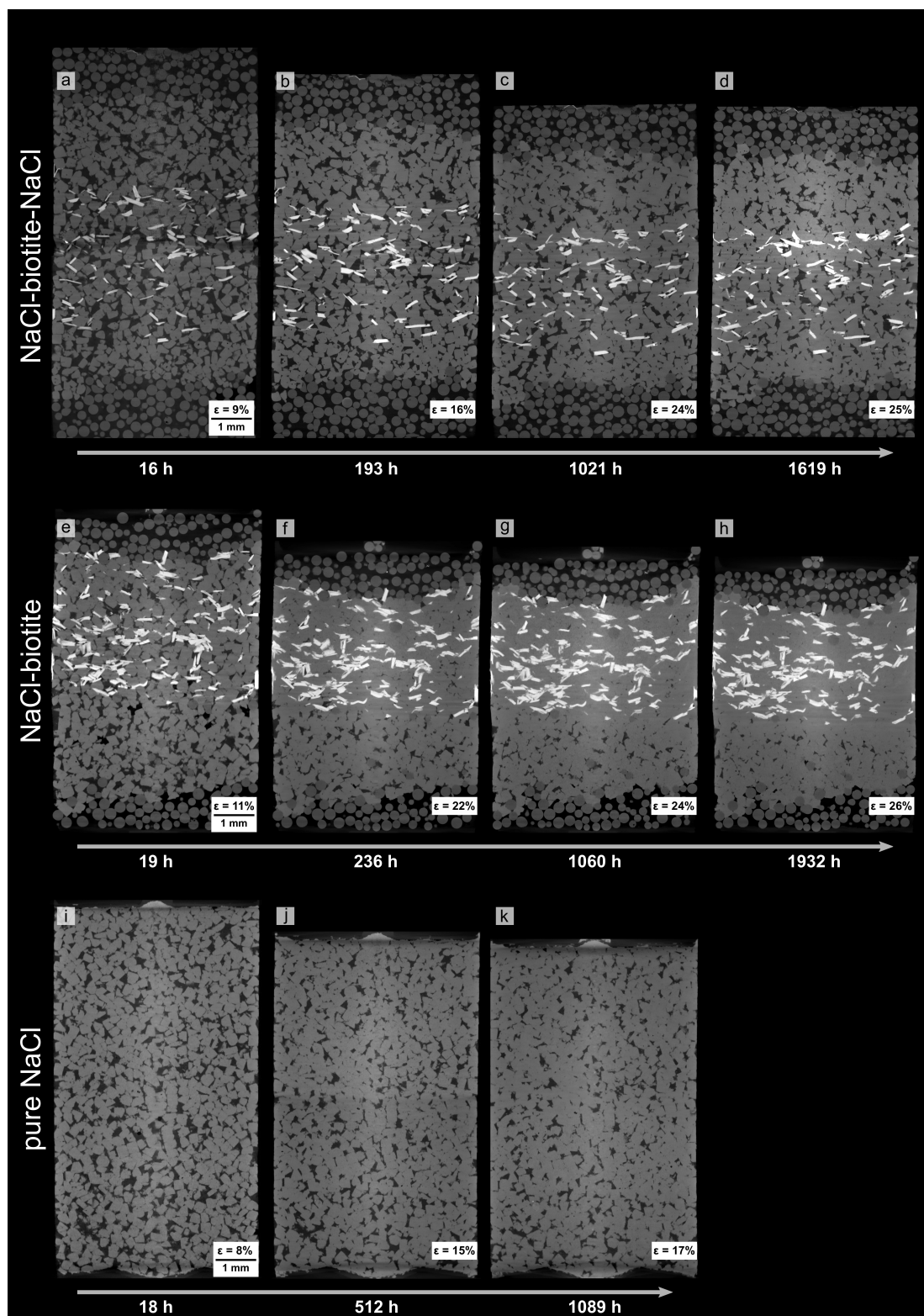
Figure 4. Vertical slices through absorption μCT scans at different stages of compaction. Different shades of grey refer to different phases present in the samples (in black: brine filled pore space, dark grey: glass beads, grey: NaCl grains and light grey: biotite) The top and middle row show the NaCl-biotite samples *SBS* (a-d) and *SB* (e-h), respectively, the bottom row displays the pure NaCl sample (i-k). b), f) and j) show first signs of porosity reduction and indentation of NaCl grains which we interpret as indicators for active dissolution precipitation creep and which is continuing throughout the experiment. Note that the final scan of the *SB* sample (h) shows no remaining porosity in the biotite-bearing layers, whereas it is still clearly visible in the *SBS* (d) and the pure NaCl sample (k).
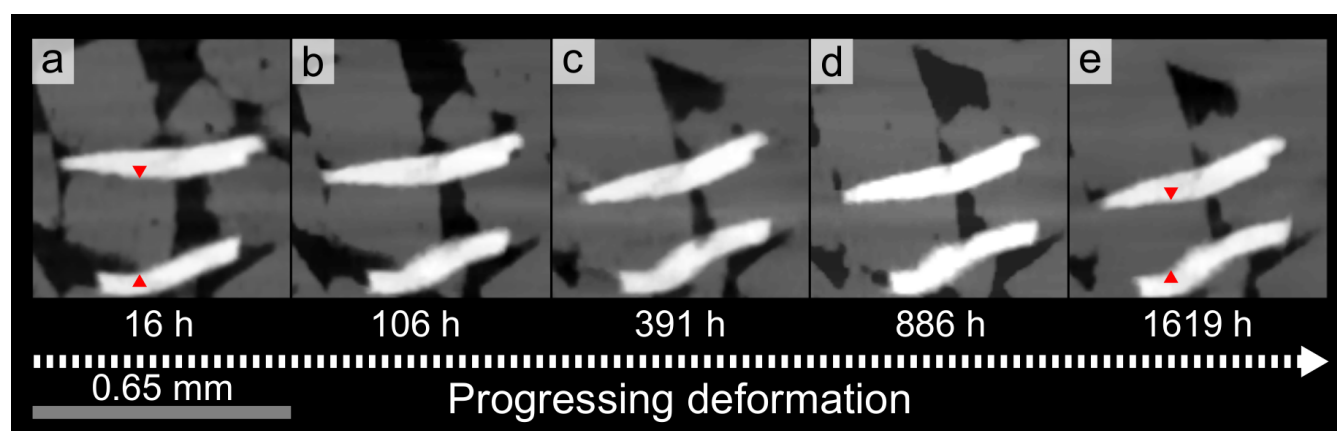

Figure 5. Sequence of time steps showing active dissolution-precipitation creep at the interphase boundaries of a NaCl grain with two biotite grains in the *SBS* sample. Comparison of a & e shows that the vertical strain accommodated by the NaCl grain is $\sim 26\%$ and contacts with the micas flattened, indicating dissolution of NaCl. Note that the biotite grains have experienced only little rotation during deformation although 1603 hrs of compaction are in between the first and the last image. The rotation of the top biotite grain occurs pre-steady state. Red arrows in a & e are used as markers for strain calculations.
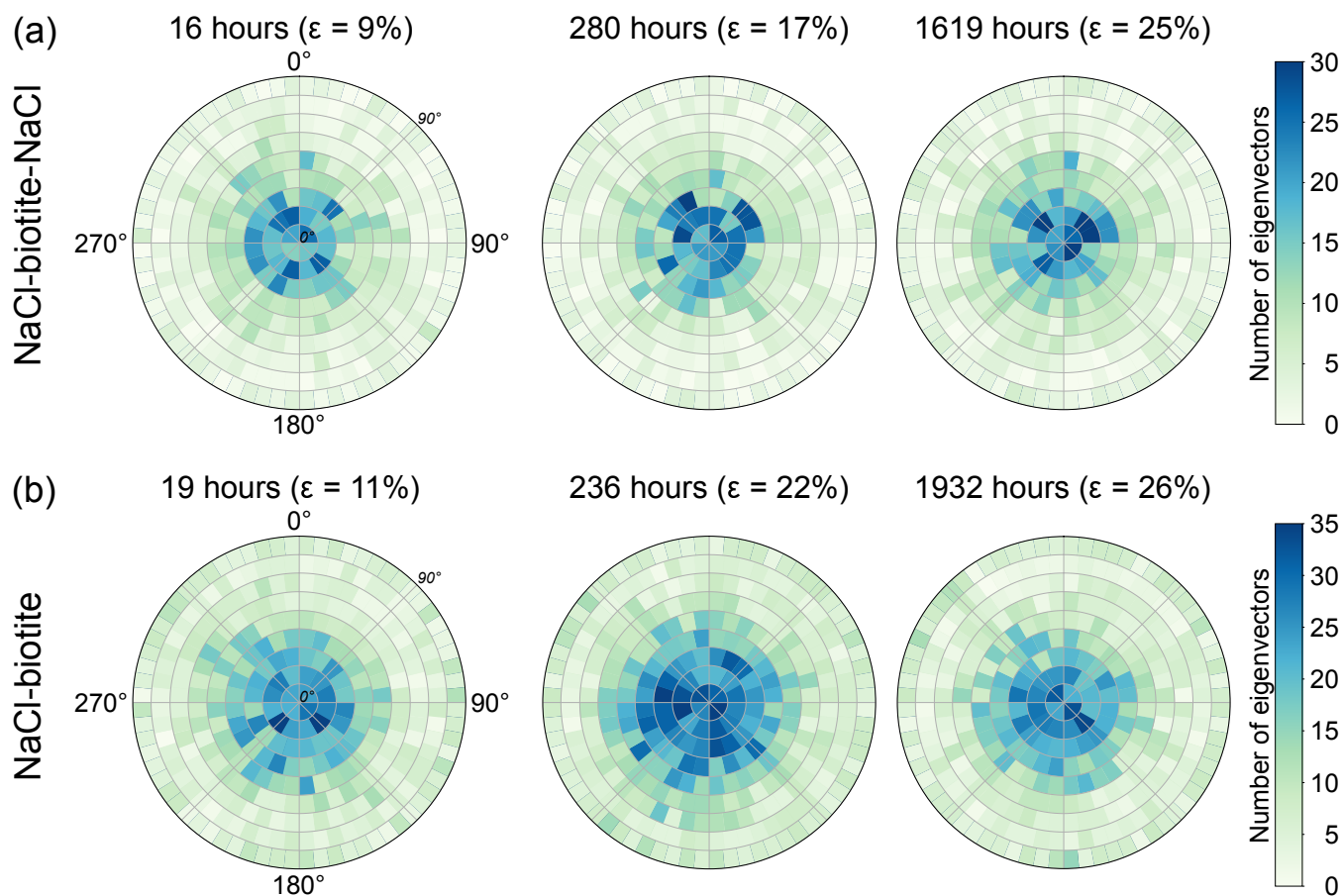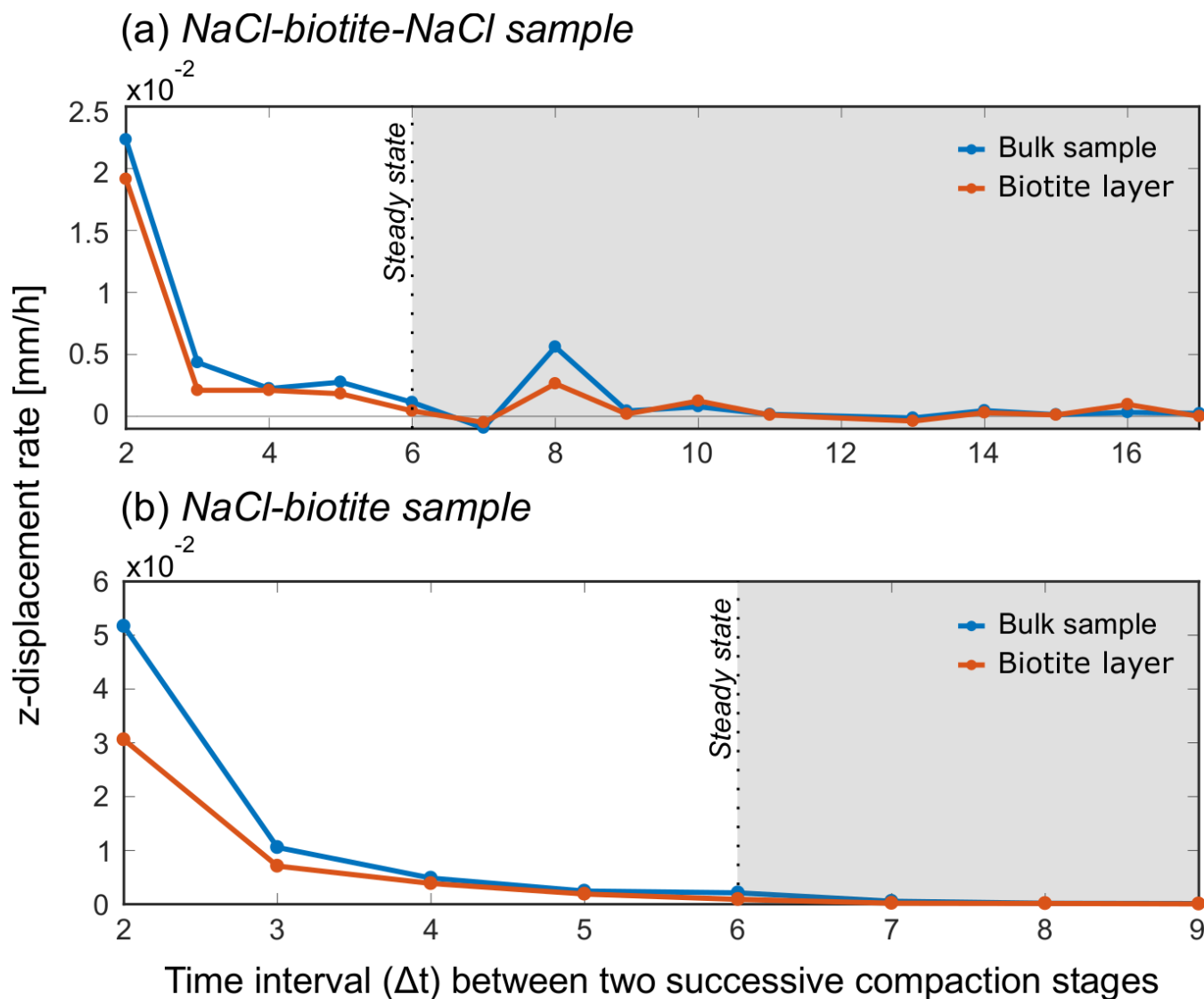
Solid Earth
Discussions

Open Access

EGU

Figure 6. Density plots of the eigenvector of biotite grains in a) the *SBS* and b) the *SB* sample. The maximum eigenvectors are plotted as densities in Lambert projections perpendicular to the basal planes of the grains. The vertical loading axis is in the centre of the plot. The rings around the central point give the angle between the vertical loading axis and the eigenvector, ranging from $0°$ in the centre to $90°$ at the outer margin. High densities of eigenvectors are displayed in blue, whereas lower densities are displayed in green. Note that the biotite grains do not change their orientation significantly with progressing deformation. For both samples, the highest densities can be found in vicinity to the central axis indicating that the majority of grains is oriented horizontally within the samples. Numbers of grains measured are from left to right for a) 1836, 1833 and 1986 and for b) 3066, 3836 and 3007.

Figure 7. The graph shows the vertical displacement rate of the bulk sample and the biotite-bearing layer, for different increments of progressing deformation over the duration of the experiments. a) contains data from the *SBS* sample and b) from the *SB* sample. During the pre-steady state deformation the bulk samples compact faster than the biotite-bearing layer. This trend continues into the steady state (grey shaded area) although both rates become comparable to each other, indicating that the biotite-bearing layer is not compacting faster than the bulk sample.

15

Solid Earth

Discussions

3.2 Strain analysis

Digital Volume Correlation (DVC) was used to analyse a locally resolved strain field and associated strain rates. Figures 8,

230 9 & 10 show the deviatoric strain and volumetric strain for the three samples at different stages during the deformation (see appendix for definition of terms). Whereas the pure NaCl sample showed a homogeneous distribution of the deviatoric and volumetric strains within the bulk sample, strain maxima in the biotite-bearing samples were located within the biotite-bearing layer, but not exclusively. Pure NaCl domains were also affected by high strains. The dominating character of the volumetric strain was negative in all three samples, indicating compaction.

235 Furthermore, we calculated average strain rates from the locally resolved strains by dividing each calculated strain value by the time interval length given in seconds. The results are displayed in Table 2 and show an overall decreasing trend in all three samples. In the two biotite-bearing samples, deviatoric strain rate maxima were homogeneously distributed, independent of the layer composition. Comparison of these results to the pure NaCl sample showed no major difference. The observed rates are comparable to the bulk strain rates (see Sect. 3.1.1).

240 In order to locate the strain maxima in 3D and compare them to the position of the biotite grains, we plotted the deviatoric and volumetric strain data of the biotite-bearing sample *SBS* on top of the segmented biotite data (Fig. 11). This showed that in the early stages of our experiment, deviatoric strain maxima corresponded to the location of biotite grains as well as open pore space and pure NaCl clusters. Later on this correlation still existed, but was less distinctive. However, local minima and maxima of the volumetric strain did not correlate with the position of biotite grains.

Table 2. Mean strain rates derived from image correlation.

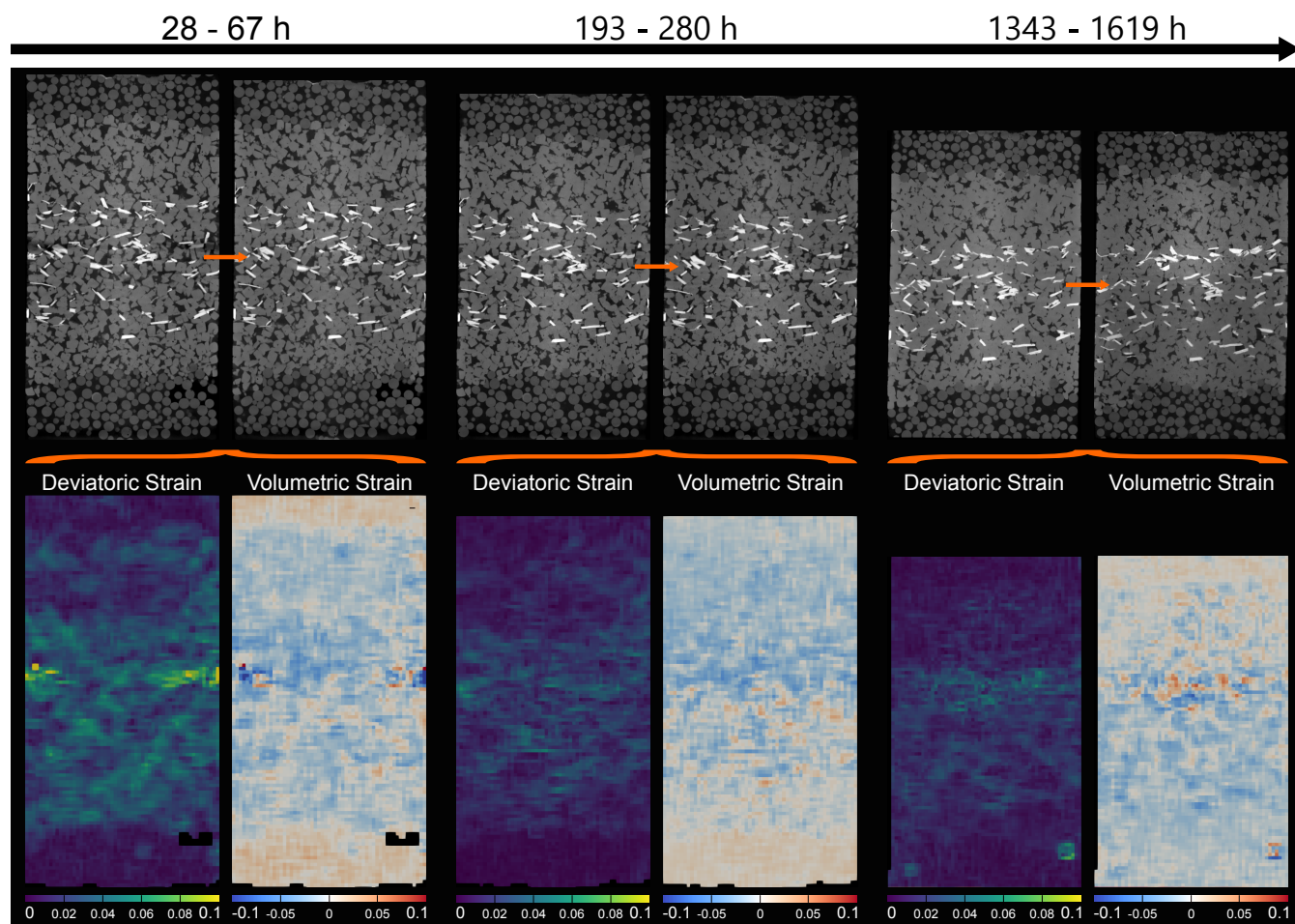| Sample	Time [h]	Deviatoric strain rate $[s^{-1}]$	Volumetric strain rate $[s^{-1}]$
SBS	28	2.0×10^{-7}	-7.0×10^{-8}
	1619	1.6×10^{-8}	-9.1×10^{-10}
SB	19	3.8×10^{-7}	-3.6×10^{-7}
	1932	7.7×10^{-9}	-3.3×10^{-8}
S1	18	2.2×10^{-7}	-1.8×10^{-7}
	1089	1.9×10^{-8}	-1.6×10^{-8}

Figure 8. Locally resolved absolute values of deviatoric and volumetric strain calculated from digital volume correlation for three different time steps. The top row shows the two microtomography scans which were compared to each other using digital volume correlation. In the bottom row, the results of the strain calculation are displayed. Note that the strains are cumulative and cover the entire time interval between the two selected scans. The duration of the time intervals increase from the left to the right and are 39 hrs, 87 hrs and 276 hrs. For the deviatoric strain bright colours represent high strains whereas dark colours represent low strains. For the volumetric strain blue indicates compaction while red indicates dilation. Note that the strains are resolved on the grain scale.
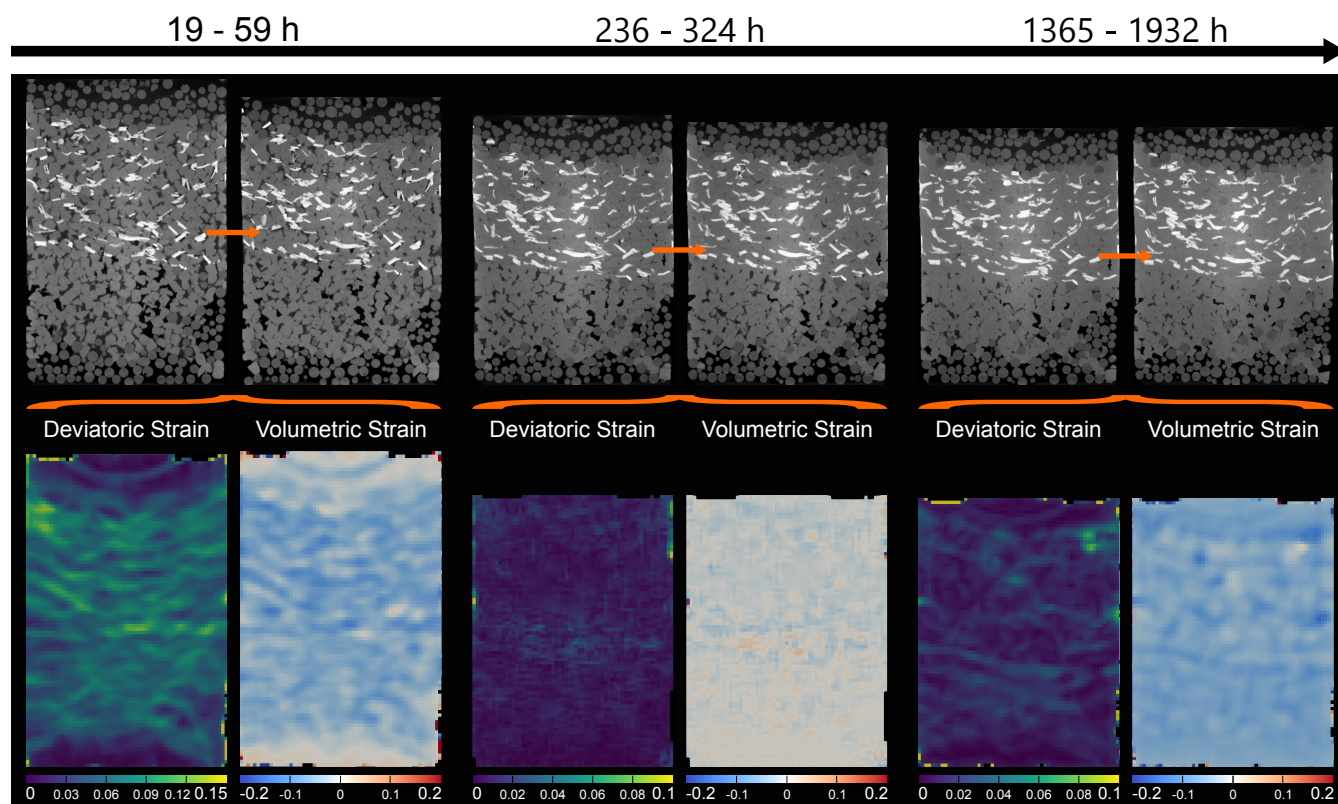
Figure 9. Locally resolved absolute values of deviatoric and volumetric strain calculated from digital volume correlation for three different time steps. The top row shows the two microtomography scans which were compared to each other using digital volume correlation. In the bottom row, the results of the strain calculation are displayed. Note that the strains are cummulative and cover the entire time interval between the two selected scans. The time intervals increase from the left to the right and are 40 hrs, 88 hrs and 567 hrs. For the deviatoric strain bright colours represent high strains whereas dark colours represent low strains. For the volumetric strain blue indicates compaction while red indicates dilation. Note the larger scale for the first time step of the deviatoric strain and that the strains are resolved on the grain scale.
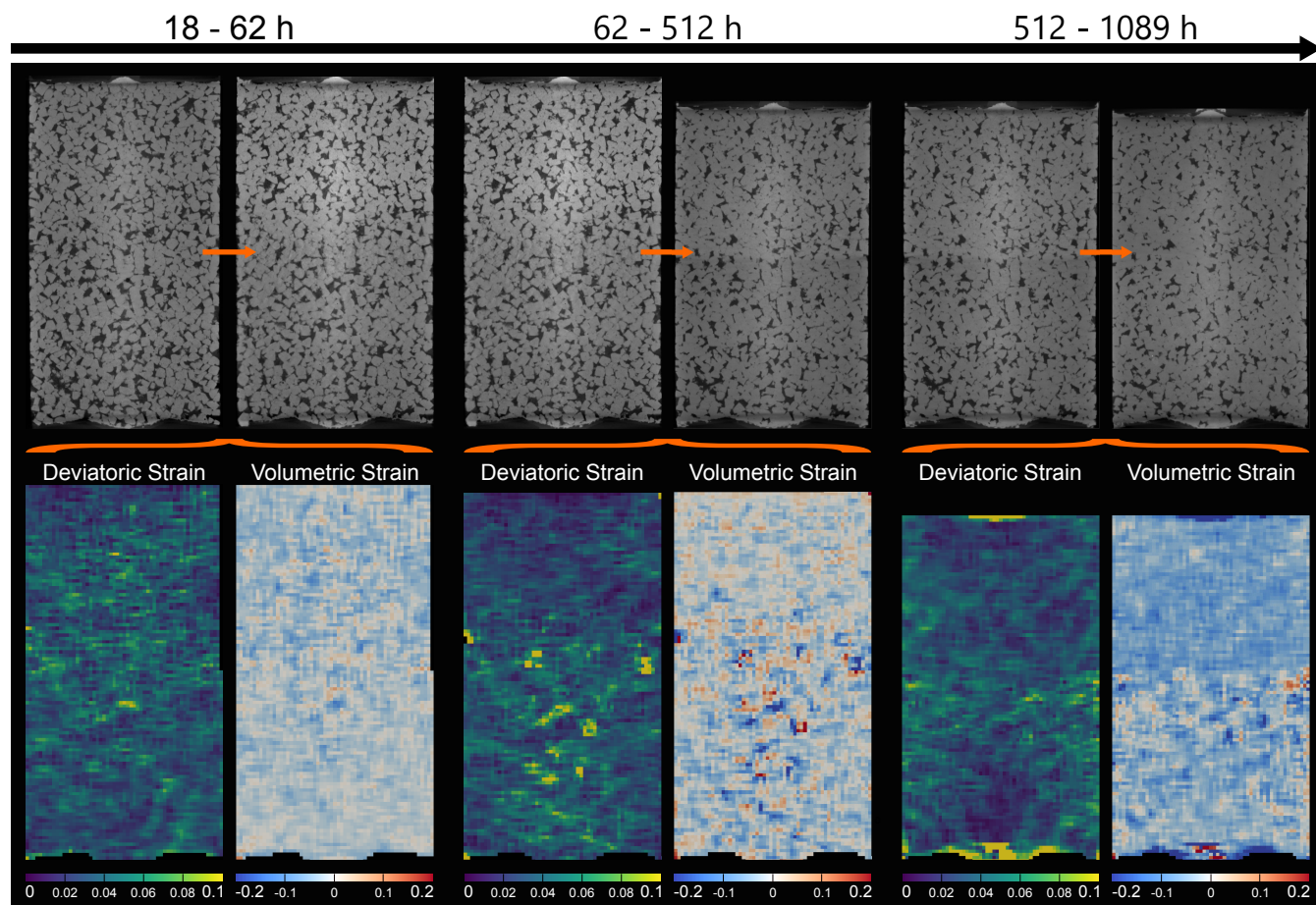
18

Figure 10. Locally resolved absolute values of deviatoric and volumetric strain calculated from digital volume correlation for three different time steps. The top row shows the two microtomography scans which were compared to each other using digital volume correlation. In the bottom row, the results of the strain calculation are displayed. Note that the strains are added up and cover the entire time interval between the two selected scans. The time intervals increase from the left to the right and are 44 hrs, 450 hrs and 577 hrs. For the deviatoric strain bright colours represent high strains whereas dark colours represent low strains. For the volumetric strain blue indicates compaction while red indicates dilation.
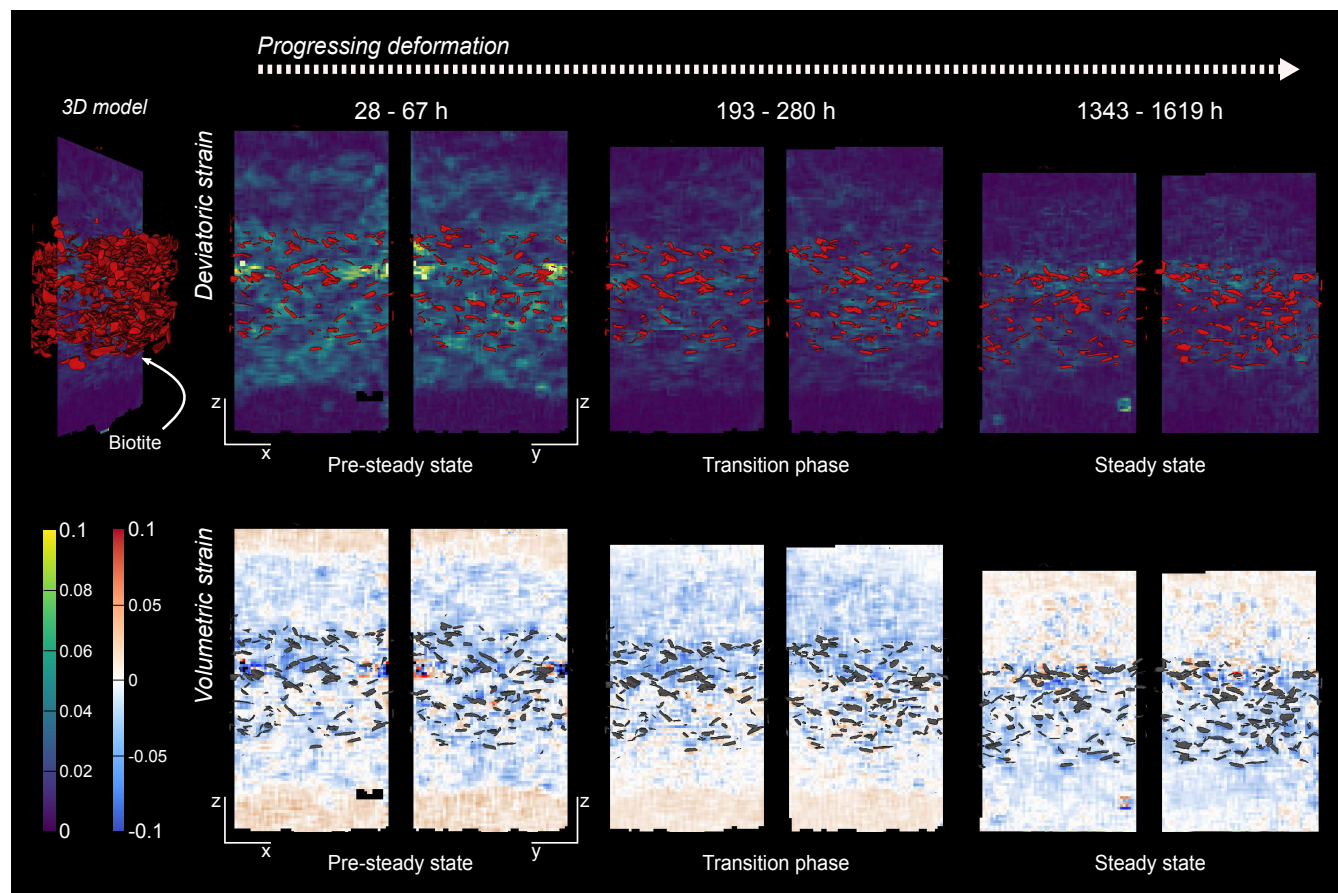
Figure 11. Comparison of the location of biotite grains with strain maxima derived from digital volume correlation. The biotite was segmented from μCT scans and plotted on top of the corresponding vertical slice through the DVC result. The top row shows the deviatoric strain and the bottom row the volumetric strain of the *SBS* sample at three different stages of deformation. Note the different orientation of slices to display the three-dimensional information. With progressing deformation the deviatoric strain is more focused in the biotite-bearing layer. However, maxima also occur in adjacent pure NaCl layers.

3.3 Porosity evolution

2-dimensional analysis of the porosity in each slice along the loading axis shows that the two biotite containing samples developed a characteristic pattern in their porosity distribution with progressing deformation. In both samples, the maximum loss of porosity correlates with the location of the biotite-bearing layer (Fig. 12 b, c). Whereas in sample *SBS* the minimum porosity did not fall below $\sim 10\%$ even after 1619 hrs, we observed compartmentalisation of *SB* into a low ($\phi \leq 2\%$) and a high ($\phi \sim 15\%$) porosity zone after 236 hrs (Fig. 12 b). In the pure NaCl sample the porosity decreased homogeneously and

did not fall below ~ 10% by the end of the experiment (Fig. 12 a). Errors for the analyses were determined as 3.8 - 7.3 % for the pure NaCl sample, 1.7 - 6.9 % for the *SBS* sample and 1.2 - 8.4% for the *SB* sample.
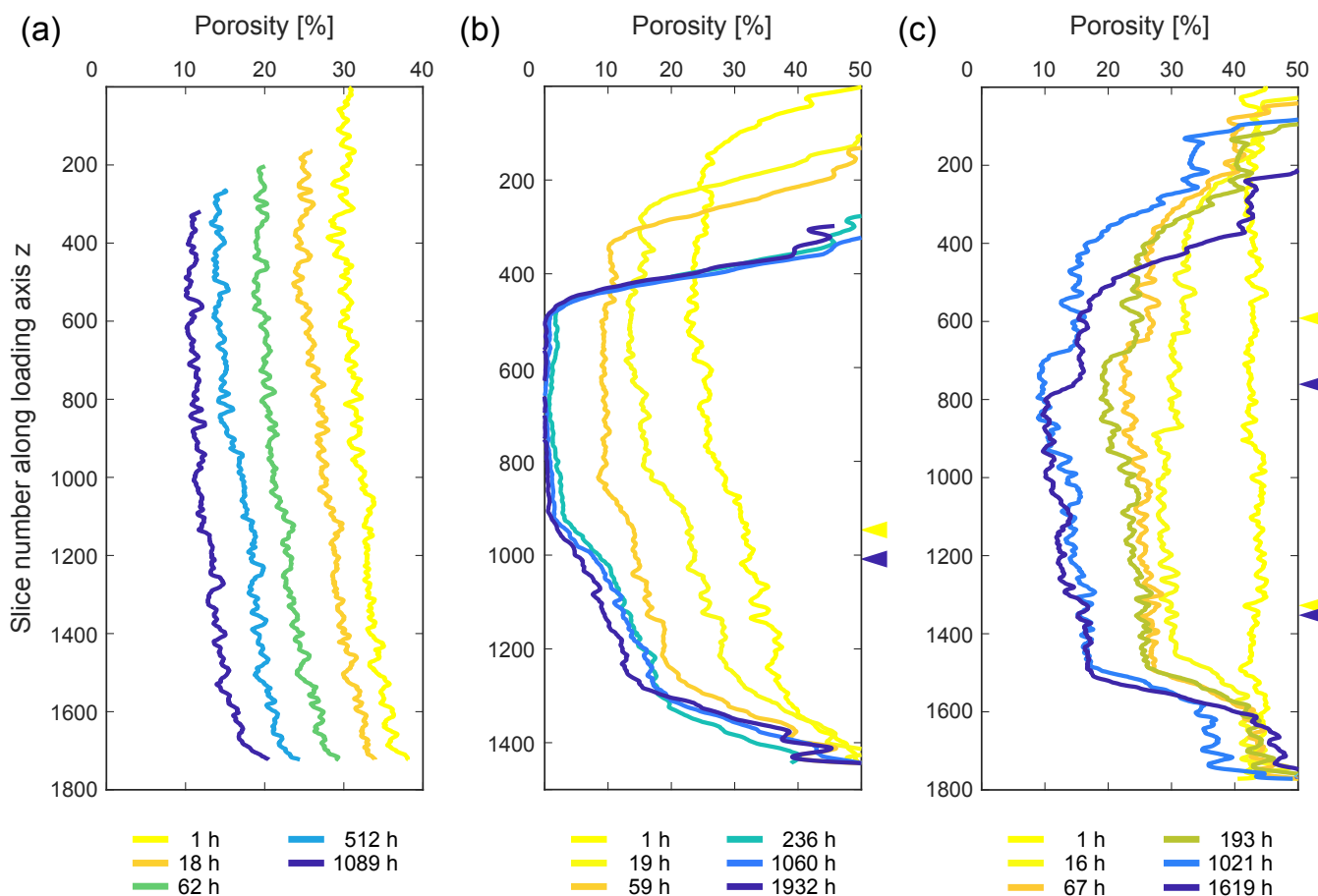

Figure 12. Porosity evolution of a) the pure NaCl, b) the *SB* and c) the *SBS* sample with progressing deformation. The porosity was measured as 2-dimensional porosity for each slice along the loading axis. Different colours indicate different time steps, ranging from yellow to blue with progressing compaction. While a) shows a homogeneous decrease of the porosity within the sample, heterogeneities arise in b) and c) which show the compositionally layered samples. The highest porosity loss occurs in biotite-bearing layers, resulting in compartmentalisation of the *SB* sample (cf. Sect. 2.5). Note that the arrows on the right hand side mark the transition from the pure NaCl domain to the NaCl-biotite domain and colours are corresponding to the deformation stage as denoted in the key.

3.4 NaCl redistribution

The changes to the relative distribution of NaCl in the three samples are shown in Fig. 13. Whereas the pure NaCl sample

255 showed a homogeneous increase of the NaCl content by ~ 13% throughout the bulk sample, a different trend could be observed in the biotite-bearing samples. While the pure NaCl layer in the *SB* sample showed an increase of NaCl by ~ 13%, which is

comparable to the pure NaCl sample, the amount of NaCl at the NaCl-biotite interface increased by $\sim 15\%$ (Fig. 13b). A similar trend could be observed in the *SBS* sample (Fig. 13c). Here, the bottom NaCl layer gained $\sim 14\%$ of NaCl and the top NaCl layer $\sim 16\%$. Notable shoulders formed at the interfaces between the pure NaCl and the NaCl-biotite layers.
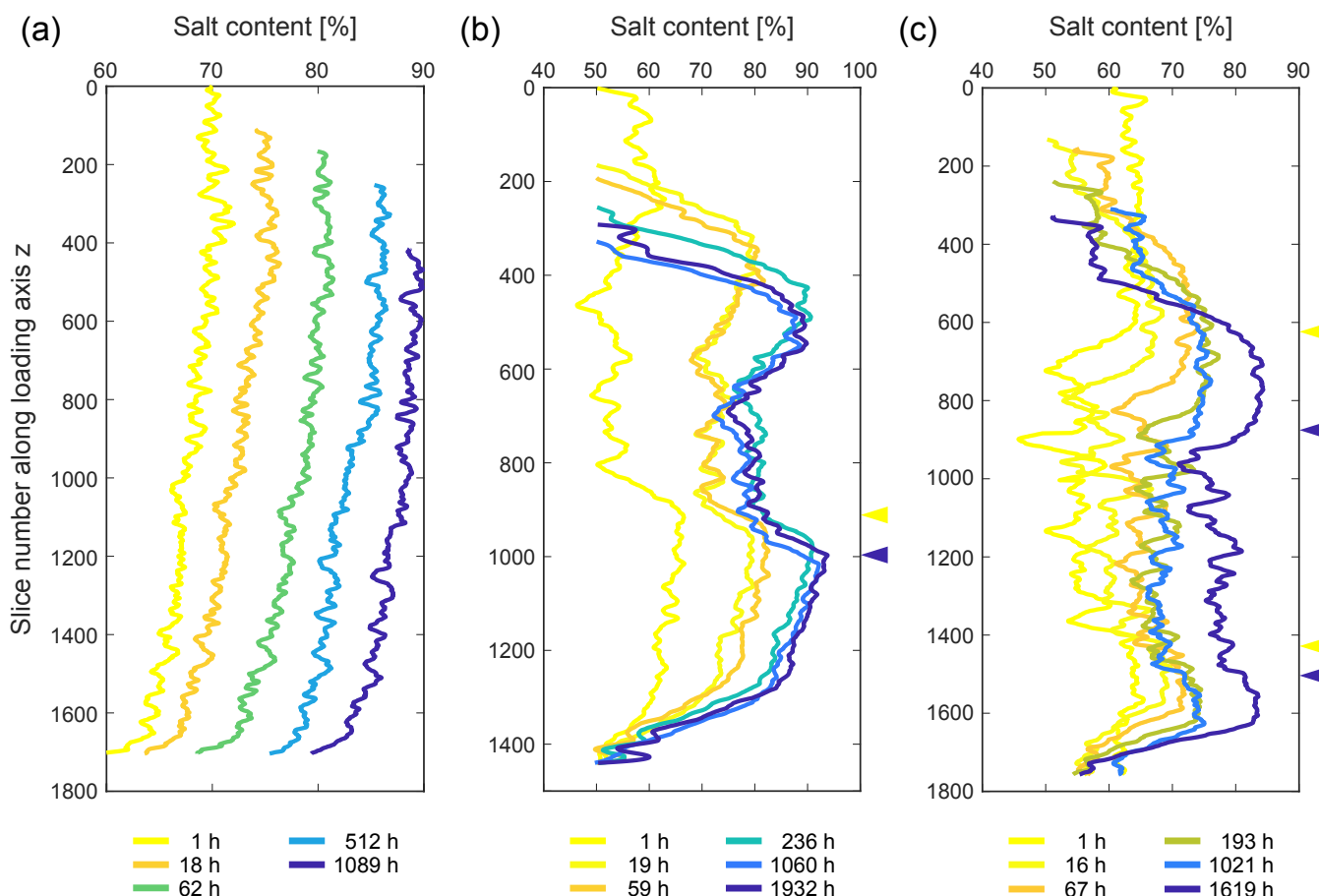

Figure 13. Evolving NaCl distribution in a) the pure NaCl, b) the *SB* and c) the *SBS* sample with progressing deformation. The NaCl content was measured in 2D for each slice along the loading axis. While a) shows a homogeneous increase of the NaCl content within the sample, b) and c) show that the NaCl-content in the biotite-bearing layer increases more than in the rest of the sample. Note that the arrows at the side mark the position of the interface between the biotite-bearing layer and the pure NaCl-layer, with their colours corresponding to the time steps as indicated in the key below.

260 Figure 14 shows volumetric analyses that determine the relative proportions of NaCl, pores and biotite in the biotite-bearing layers. In these analyses, biotite acts as an insoluble internal standard. Errors for the measurements were determined from the accuracy of the AI segmentation and are represented by a shaded area around the line plot. Both samples show that, while the biotite content is indeed constant within the analysed sub-volumes, the relative reduction of porosity is compensated by a

relative increase in the NaCl content in these volumes. In the *SBS* sample, just over 10% of additional salt were measured in

265 the biotite-bearing layer, with a slightly lower increase in the *SB* sample.
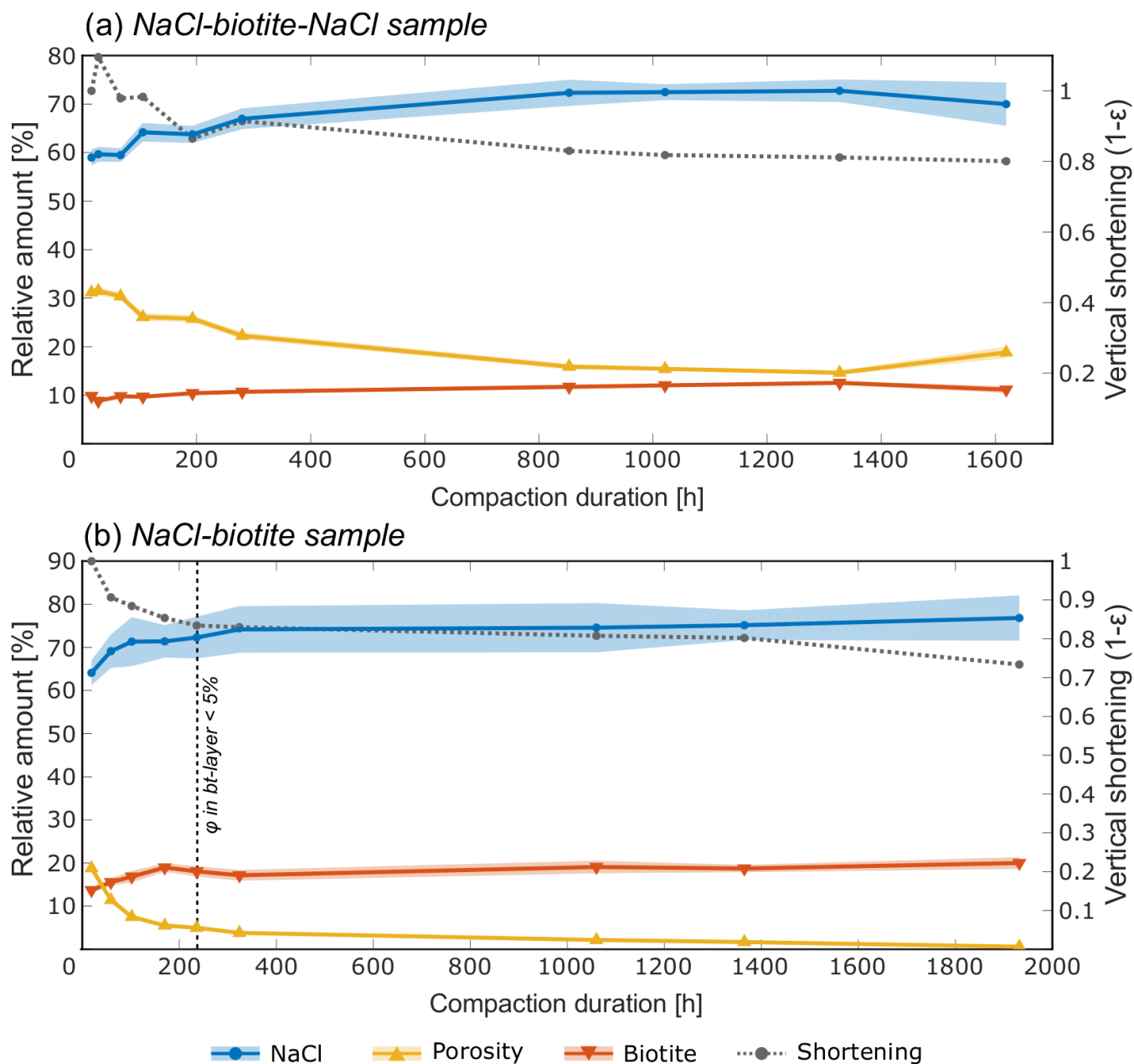
Figure 14. Evolution of the relative volumes of NaCl, biotite and porosity in the biotite-bearing layers of a) the *SBS* and b) the *SB* sample, with progressing deformation. In both samples the biotite-content remains constant within the segmentation error while the NaCl content increases and the porosity decreases. This is persistent throughout the experiment. After 324 hours of compaction the increase of the NaCl content in the *SB* sample (b) stagnates, which corresponds to the breakdown of porosity in the biotite-bearing layer.

4   Discussion

4.1   Length scales of NaCl transport during DPC

The experiments allowed us to compare bulk compaction of the samples to deformation on the grain scale in three different samples over a total duration of 1089 (pure NaCl), 1619 (*SBS*) and 1932 hrs (*SB*). The general compaction behaviour we

270   observed was consistent with previous studies on NaCl compaction (Spiers and Schutjens, 1990; Renard et al., 2004; Macente et al., 2018). Independent of the sample composition, the compaction was accomplished by an asymptotic decrease of the bulk strain rate. These observations indicate a change in deformation mode after 200 hours of compaction. We interpret the non-linear character of our compaction and strain rate curves to display the transition from mixed mechanical and chemical compaction to chemical compaction early on, as well as the establishment of a steady state deformation after 200 hours of

275   compaction. Microstructural observations, which showed enhanced indentation of NaCl grains and reduction of pore space with progressing deformation (Fig. 5), point to the activity of dissolution-precipitation creep (e.g. Rutter (1983); Tada and Siever (1989); Gratier et al. (2013)) during that period.

Visualisation of our results show that the compaction was accommodated across the entire biotite-bearing samples (Figs. 7, 8 & 9), which is in conflict with models that postulate a pronounced effect of phyllosilicates on deformation localisation

280   (Heald, 1956; Thomson, 1959; Aharonov and Katsman, 2009) and acceleration of compaction (Hickman and Evans, 1995; Rutter and Wanten, 2000). We tested this observation by comparing the vertical displacement rates within the sample to the bulk compaction rate, and by calculating locally resolved strains using digital image correlation. While we found that the biotite-bearing layers did not compact faster than the bulk samples, we also found that high deviatoric and volumetric strains were not restricted to the biotite-bearing layers. In fact, pure NaCl domains in biotite-bearing samples showed similar strain

285   patterns (Figs. 8, 9 & 10), and the overall strain distribution in these samples was comparable to the one observed in the pure NaCl reference sample. Therefore, we conclude that deformation was not localised in the biotite-bearing layer but distributed and accommodated across all layers. Macente et al. (2018) came to a similar conclusion, explaining their results with a stress bearing network of *dynamic force chains* in the pure NaCl domains which evolve in the granular material as response to a feedback of applied vertical loading and the increase in load-bearing cross sectional area due to local variations in the

290   dissolution rate (Bruthans et al., 2014). Furthermore, they concluded that deformation was promoted by phase boundaries in the biotite-bearing layer. Similar to Macente et al. (2018), we observed the highest porosity reduction in layers containing phyllosilicates. Compared to the pure NaCl layers, these layers lost $\sim 24\%$ more in the *SBS*, and $\sim 41\%$ more in the *SB* sample relative to the initial porosities in each layer. Combining the observations of higher porosity loss in the biotite-bearing layers with the evidence that compaction is not concentrated in those layers leads to a paradox that cannot be explained by the

295   classical theory of DPC, which would suggest enhanced DPC to lead to strain localisation and thus a porosity loss. A possible solution would be diffusive material transport from a source outside the biotite-bearing layer into the pore space of that layer.

We were able to show that the NaCl content in the biotite-bearing layers of the *SB* and *SBS* sample increased with progressing deformation (cf. Figs. 13 & 14) and we interpret this salt to have been sourced from the pure NaCl layers. In the *SB* sample the largest effect can be observed at the layer interface from which a negative gradient emerged towards the top of the biotite-

300 bearing layer (Fig. 13b). In this case the effect of the NaCl migration is restrained by the breakdown of porosity after 170 hours which limits further migration of dissolved NaCl into the biotite-bearing layer from the suspected source in the pure NaCl layer at the bottom of the sample (Fig. 13b). In the *SBS* sample, we see no porosity breakdown and no gradient in the NaCl distribution emerge within the biotite-bearing layer. The porosity remains interconnected throughout the entire experiment, maintaining access to both NaCl layers as potential sources for salt. The biotite-bearing layer showed a consistently higher

305 increase in NaCl than the marginal pure NaCl layers (Fig. 13c). Especially the upper NaCl layer did develop a pronounced gradient towards the interface with the biotite-bearing layer though, which could be evidence for a diffusive salt redistribution. Combined, we consider these observations strong evidence for NaCl diffusion over multiple grain diameters into the biotite-bearing layer.

Merino et al. (1983) proposed a model that could explain our observations of long-distance diffusive NaCl redistribution

310 in the samples. They suggest that a locally increased porosity leads to reduced contact areas of grains and consequently higher local stresses along these contacts. In DPC, this causes an increased chemical potential and shift from an equilibrium between the fluid and the salt towards conditions that favour dissolution. Hence, the concentration of dissolved matter in the local pore fluid is increasing and diffusion occurs along a concentration gradient towards domains with a lower porosity, in our samples the biotite-bearing layers. There, due to lower local stresses at the grain contacts, the equilibrium concentration

315 of the solute is reduced and precipitation in the open pore space occurs. For Merino's model to be applicable, the NaCl supersaturations produced by pressure solution must be maintained over transport distances greater than the grain scale before redeposition. Experiments by Desarnaud et al. (2014) demonstrate that, counter-intuitively, large supersaturations of NaCl (up to $1.6\times$) can persist in aqueous solutions before nucleation. Furthermore, Zimmermann et al. (2015) use atomistic simulations to demonstrate that the nucleation kinetics of NaCl are controlled by desolvation rather than diffusive transport.

320 We explain the initial porosity variation that is needed for Merino et al.'s feedback model with differences in shapes and sizes between the NaCl and biotite grains, where biotite-bearing layers experienced greater earlier compaction than the pure NaCl layers (Fig. 12), leading to lower initial porosity. If the model applies to our results, this would in turn imply that driving forces for transport during DPC even in the absence of advective transport are more diverse than diffusion on the grain scale alone, and thus more complex than classical models suggest (e.g. Raj, 1982; Rutter, 1983; Gratier, 1987).

325 This is in accordance with field observations by Heald (1956), Mimran (1977) and Buxton and Sibley (1981), who report observations that challenge the classical theory of precipitation in the vicinity of dissolution sites and invoke larger transport distances in Sandstones, Chalk and Limestones, respectively.

4.2   What is the role of the biotite?

Our DVC analysis revealed that a proportion of the maxima in the grain-scale shear strains (cf. Figs. 8 & 9) corresponded to

330 biotite-NaCl phase boundaries. Such phase boundaries are characterised by significant electrochemical effects (Walderhaug et al., 2006; Greene et al., 2009; Kristiansen et al., 2011), which likely accelerate dissolution of NaCl. Visualising such interfaces from our data showed the efficiency of this process (cf. Fig. 5). At the same time, our label analysis showed that biotite grains did not rotate significantly (Fig. 6). Especially during the early stages of compaction, where the sample still had a high
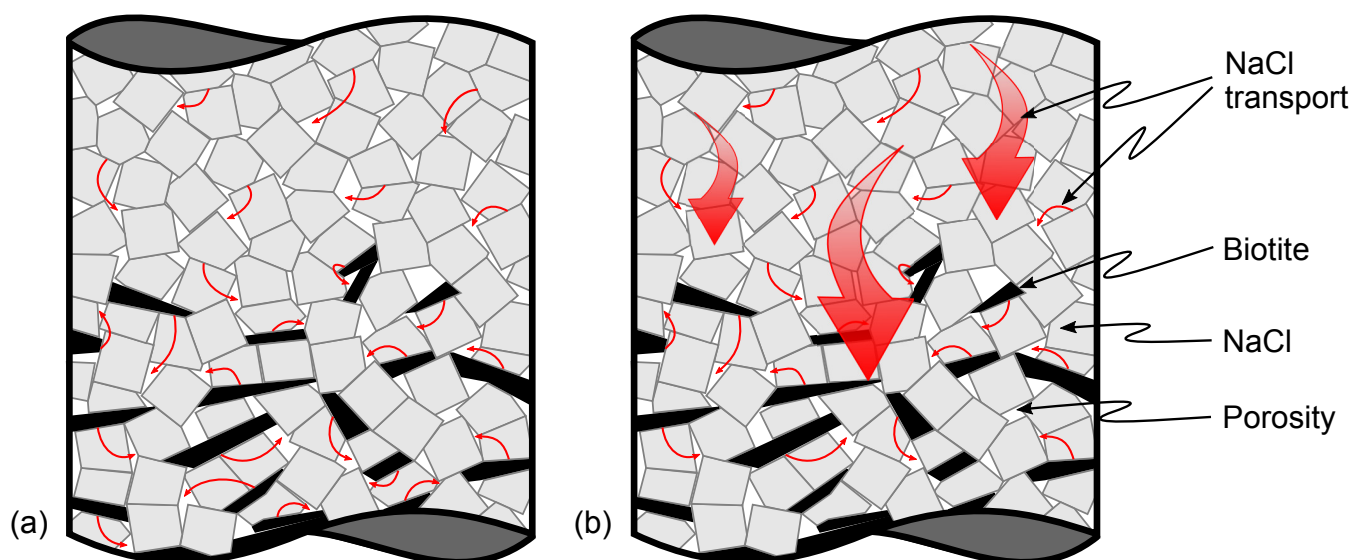
Figure 15. Possible transport length scales during dissolution-precipitation creep as proposed with in the scope of this work. In a) Diffusion occurs only on the grain scale as described in the classical literature. In b) we added diffusive transport on longer length scales as described in Merino et al. (1983). However, diffusive transport on the grain scale is considered to be active as well.

porosity, we would expect point loading to force biotite grains to realign. We interpret the fact that this did not happen as
335 corroborating evidence for the efficiency of dissolution at biotite-NaCl phase boundaries.

An increased efficiency of dissolution along phase boundaries would imply that the biotite-bearing layers should compact preferentially. This is an effect that we clearly did not observe in our data (see previous subsection and Figs. 7, 8 & 9), which raises the question as to how the preferred dissolution is being balanced. We interpret this to happen in the following way: NaCl that is being dissolved at a biotite-NaCl phase boundary, or also along a NaCl grain boundary in the biotite-bearing layer,
340 is only redistributed locally, within that layer, so that the net volume of that layer is preserved. In the absence of advective transport in our experiment, this is in line with classical DPC theory (e.g. Paterson, 1973; Raj, 1982; Rutter, 1983; Gratier, 1987; Groshong Jr, 1988). This effect is supported by the diffusive potential described above and the additional NaCl that migrates into the layer (see previous subsection), whereby the additional NaCl contributes to a load-bearing framework whose compaction rate is in sync with the bulk sample's.
345 We do note that the biotite composition does not seem to have a first order effect on pressure solution at its interfaces: while the biotite that Macente et al. (2017; 2018) used had a composition of
$K_{0\cdot9}(Mg_{2\cdot5}Fe_{0\cdot4}Al_{0\cdot1}Ti_{0\cdot1})(Si_{2\cdot9}Al_{1\cdot1})O_{10}(OH)_2$, the one used in this study was richer in iron
$(K_{0\cdot7}Ca_{0\cdot1}(Fe_{2\cdot1}Mg_{0\cdot3}Ti_{0\cdot2})(Si_{2\cdot5}Al_{1\cdot1})O_{10}(OH)_2$, (see Table A2 in the appendix for full compositions). Both cation sites are enclosed within the crystal structure of the biotite and are not exposed at the surface of the basal plane. As the latter is

350 likely to be the reactive surface in our dissolution-precipitation creep experiments, the observed differences in composition do not affect the dissolution of matter.

In summary, while biotite grains locally are effective facilitators for DPC irrespective of their composition, it also appears that the chemo-mechanical effect on the entire system is limited and probably outperformed by the trans-domain diffusion outlined above.

4.3 A detailed discussion of our DVC analyses

4.3.1 Magnitudes of local strains

Our DVC analyses resolve deviatoric and volumetric strains on the grain scale (Figs. 8-11), and provide insights into the micromechanics of compaction in the various samples. Comparing the strains in the *SBS* with the *SB* sample showed the effect of the larger load that was used in the later compaction experiment; the maximum volumetric and deviatoric strains reached in 360 the *SB* samples are about twice as high.

4.3.2 Character of local strains & their location relative to phyllosilicates

In all three samples the dominating local *volumetric strain* was negative. This trend is persistent throughout the experiments and in line with the bulk deformation and vertical shortening of the samples. Deviations from this trend occured in the glass bead layers (cf. paragraph below) and at sites where porosity was reduced by precipitation of dissolved material. Combined, these 365 strains reflect the deformation of the samples by active DPC, tracking the volume changes of the NaCl grains and porosity. The local maxima of the volumetric strain (in red) did not correlate with the location of biotite grains but with sites of precipitation (cf. Fig. 11). However, a pronounced concentration of compaction as described in Macente et al. (2018) cannot be observed.

Deviatoric strain maxima on the other hand showed a certain correlation to the position of biotite grains, but not exclusively. Elevated deviatoric strains were also found in the pure NaCl domains, in vicinity to the biotite-bearing layer show as well 370 elevated strains. It could be argued that deviatoric strain maxima represent the mechanical sliding of grains past each other in an unconsolidated polycrystalline aggregate. However, the process causing the strain maxima continued during the steady state deformation. We rather relate these strain maxima to grain boundary sliding assisting and promoting dissolution and precipitation processes along grain boundaries independent of the sample composition.

The glass beads layer at the top and bottom of the biotite-bearing samples showed positive volumetric strains where we 375 would rather expect the volumetric strain in an incompressible medium to be zero as no volume change occurs. However, under 1-dimensional compression and when the strains are large, the isotropic strain describes a mathematical property of the strain tensor (ϵ) rather than a volume change. The volume change for incompressible materials under axial shortening can be described as

$$\frac{V_{\mathrm{F}}}{V_0} = (1+\varepsilon_1)(1+\varepsilon_3)^2 = 1 \tag{8}$$

Solid Earth
Discussions

Open Access

EGU

380   with

$$\varepsilon_2 = \varepsilon_3 \tag{9}$$

ε_1, ε_2 and ε_3 denote the maximum, intermediate and minimum strain, V_0 the initial volume and V_F the final volume. We can calculate ε_3 as function of ε_1 using

$$\varepsilon_3 = \sqrt{\frac{1}{1+\varepsilon_1} - 1} \tag{10}$$

385   Hence, the isotropic strain ($\varepsilon_{\mathrm{iso}}$) concludes to

$$\varepsilon_{\mathrm{iso}} = \frac{1}{3} tr(\epsilon) = \frac{1}{3}\varepsilon_1 + \frac{2}{3}\left(\sqrt{\frac{1}{1+\varepsilon_1}} - 1\right) \tag{11}$$

For large strains with $\varepsilon_1 \neq 0$, $\varepsilon_{\mathrm{iso}}$ is positive although the volume is not changing. Our measurements reflect this and show counterintuitive positive values in the incompressible glass beads layer.

4.3.3   The use of DVC in changing samples

390   In our analysis, we used continuum DVC to analyse samples that are changing, which violates a core assumption of image correlation, that of the preservation of mass. The fact that material gets dissolved and re-precipitated elsewhere should, in principle, cause problems with convergence of the algorithm. However, across all analysed datasets and increments, the analysis did correlate very well (videos S2 in supplementary material), with only negligible proportions of the volumes not correlating. This observation was persistent across all analysed data.

395   DVC is very sensitive to the choice of input parameters *half-window size* and *node spacing* which must be adapted to the underlying microstructure – here both of these parameters were carefully tuned to the grain size. Biotite is nonreactive on the scale of our observations and can thus be expected to correlate well. Interiors of NaCl grains are not changing during DPC, which means that the algorithm can confidently correlate volumes there. Further, during compaction, the relative proportion of grains versus pores was changing in favour of the former, which will inevitably render the correlation more robust. Lastly,

400   the relative local changes in the microstructure in the investigated intervals were moderate. We consider the combination of these parameters responsible for the successful correlation in our DVC analyses and thus conclude that the application of the technique in our samples is possible.

5   Conclusions

In this study, we have investigated active dissolution-precipitation creep in closed NaCl-biotite systems and its contribution

405   to the dynamic evolution of petrophysical rock properties during diagenesis. Our findings indicate that the presence of phyllosilicates enhances porosity reduction but has no obvious effect on deformation localisation, as compaction is accommodated in all layers and local strain maxima are homogeneously distributed within the samples. Following Merino et al. (1983) we explain this paradox with diffusive material migration exceeding the grain scale, from sources in the marginal pure NaCl-layer

to sinks in the central biotite-bearing layer. This invites a renewed discussion on the influence of phyllosilicates and the driving

410   forces for material transport during dissolution-precipitation creep with direct implications to diagenetic compartmentalization

of rocks and stylolite formation.

Appendix A

A1   Acquisition parameter for x-ray microtomography scans

Table A1. Acquisition parameter for x-ray microtomography scans.

	SBS		SB	S2
Scan parameters	**Scan 1 to 8**	**Scan 9 to 19**	**Scan 1 to 10**	**Scan 1 to 5**
Acceleration voltage	100 kV		120 kV	120kV
Target power	2.8 W			
No. of projections	2000			
Exposure time	2 s			
Source to sample distance	19.5 mm	18.25 mm	19.25 mm	
Source to camera distance	705.75 mm	706.25 mm	712.8 mm	
Duration of scan	67 min			
Filter	0.3 mm Al-filter			
10 dark current & 10 flat field images	yes		yes	yes
Voxel size	0.005469 mm	0.005115 mm	0.005346 mm	0.005346 mm

A2   Definition of strain as used in DVC

415   The strain tensor is composed of an isostatic and deviatoric component. While the isostatic component is equal to the volumetric

strain and describes a change in volume, the deviatoric strain describes the deformation at constant volume (cf. Sect. 2.6).

A3 XRF analysis of biotite

Table A2. XRF analysis of mica used in our experiments (Bt-BS) and in Macente (2017) (Mc-AM). Values are given in weight%

Sample	Bt-BS	Mc-AM
SiO_2	35.29	42.52
TiO_2	2.941	0.90
Al_2O_3	12.60	14.30
Fe_2O_3	35.68	6.28
MnO	0.381	0.06
MgO	2.99	24.19
CaO	1.32	0
Na_2O	0.07	0
K_2O	7.647	10.39
P_2O_5	0.091	0.01
LOI	0.81	0.77
Total	99.83	99.42

References

Aharonov, E. and Katsman, R.: Interaction between pressure solution and clays in stylolite development: Insights from modeling, Am. J.
Sci., 309, 607–632, https://doi.org/https://doi.org/10.2475/07.2009.04, 2009.

Arganda-Carreras, I., Kaynig, V., Rueden, C., Eliceiri, K. W., Schindelin, J., Cardona, A., and Sebastian Seung, H.: Train-
able Weka Segmentation: a machine learning tool for microscopy pixel classification, Bioinformatics, 33, 2424–2426,
https://doi.org/https://doi.org/10.1093/bioinformatics/btx180, 2017.

Bons, P. D. and Urai, J. L.: Experimental deformation of two-phase rock analogues, Mater. Sci. Eng. A, 175, 221 – 229,
https://doi.org/https://doi.org/10.1016/0921-5093(94)91061-8, 1994.

Bruthans, J., Soukup, J., Vaculikova, J., Filippi, M., Schweigstillova, J., Mayo, A. L., Masin, D., Kletetschka, G., and Ri-
hosek, J.: Sandstone landforms shaped by negative feedback between stress and erosion, Nature Geosci, 7, 597–601,
https://doi.org/https://doi.org/10.1038/ngeo2209, 2014.

Buades, A., Coll, B., and Morel, J.-M.: Non-local means denoising, Image Process. Line, 1, 208–212,
https://doi.org/https://doi.org/10.5201/ipol.2011.bcm_nlm, 2011.

Buxton, T. M. and Sibley, D. F.: Pressure solution features in a shallow buried limestone, J. Sediment. Res., 51, 19–26,
https://doi.org/https://doi.org/10.1306/212F7BF8-2B24-11D7-8648000102C1865D, 1981.

Coble, R.: A model for boundary diffusion controlled creep in polycrystalline materials, Int. J. Appl. Phys, 34, 1679–1682,
https://doi.org/https://doi.org/10.1063/1.1702656, 1963.

Croize, D., Renard, F., and Gratier, J.-P.: Compaction and porosity reduction in carbonates: A review of observations, theory, and experiments,
in: Advances in Geophysics, vol. 54, pp. 181–238, Elsevier, https://doi.org/https://doi.org/10.1016/B978-0-12-380940-7.00003-2, 2013.

Desarnaud, J., Derluyn, H., Carmeliet, J., Bonn, D., and Shahidzadeh, N.: Metastability Limit for the Nucleation of NaCl Crystals in Con-
finement, J. Phys. Chem. Lett., 5, 890–895, https://doi.org/https://doi.org/10.1021/jz500090x, 2014.

Dierick, M., Masschaele, B., and Van Hoorebeke, L.: Octopus, a fast and user-friendly tomographic reconstruction package developed in
LabView®, MST, 15, 1366, https://doi.org/10.1088/0957-0233/15/7/020, 2004.

Durney, D.: Solution-transfer, an important geological deformation mechanism, Nature, 235, 315,
https://doi.org/https://doi.org/10.1038/235315a0, 1972.

Durney, D.: A Discussion on natural strain and geological structure-Pressure-solution and crystallization deformation, Philos. Trans. Royal
Soc. A, 283, 229–240, https://doi.org/https://doi.org/10.1098/rsta.1976.0081, 1976.

Gratier, J.: Pressure solution-deposition creep and associated tectonic differentiation in sedimentary rocks, Geol. Soc. Spec. Publ., 29, 25–38,
https://doi.org/https://doi.org/10.1144/GSL.SP.1987.029.01.03, 1987.

Gratier, J.-P., Dysthe, D. K., and Renard, F.: The role of pressure solution creep in the ductility of the Earth's upper crust, in: Advances in
Geophysics, vol. 54, pp. 47–179, Elsevier, https://doi.org/https://doi.org/10.1016/B978-0-12-380940-7.00002-0, 2013.

Green, H.: "Pressure solution" creep: some causes and mechanisms, J. Geophys. Res. Solid Earth, 89, 4313–4318,
https://doi.org/https://doi.org/10.1029/JB089iB06p04313, 1984.

Greene, G. W., Kristiansen, K., Meyer, E. E., Boles, J. R., and Israelachvili, J. N.: Role of electrochemical reactions in pressure solution,
Geochim. Cosmochim. Acta, 73, 2862 – 2874, https://doi.org/https://doi.org/10.1016/j.gca.2009.02.012, 2009.

Groshong Jr, R. H.: Low-temperature deformation mechanisms and their interpretation, Geol. Soc. Am. Bull., 100, 1329–1360,
https://doi.org/https://doi.org/10.1130/0016-7606(1988)100<1329:LTDMAT>2.3.CO;2, 1988.

460   Gundersen, E., Renard, F., Dysthe, D. K., Bjørlykke, K., and Jamtveit, B.: Coupling between pressure solution creep and diffusive mass transport in porous rocks, J. Geophys. Res. Solid Earth, 107, ECV–19, https://doi.org/https://doi.org/10.1029/2001JB000287, 2002.

Heald, M. T.: Cementation of Simpson and St. Peter sandstones in parts of Oklahoma, Arkansas, and Missouri, J. Geol, 64, 16–30, https://doi.org/https://doi.org/10.1086/626314, 1956.

Herring, C.: Diffusional viscosity of a polycrystalline solid, Int. J. Appl. Phys, 21, 437–445,
465   https://doi.org/https://doi.org/10.1063/1.1699681, 1950.

Hickman, S. H. and Evans, B.: Kinetics of pressure solution at halite-silica interfaces and intergranular clay films, J. Geophys. Res. Solid Earth, 100, 13 113–13 132, https://doi.org/https://doi.org/10.1029/95JB00911, 1995.

Kristiansen, K., Valtiner, M., Greene, G. W., Boles, J. R., and Israelachvili, J. N.: Pressure solution–The importance of the electrochemical surface potentials, Geochim. Cosmochim. Acta, 75, 6882–6892, https://doi.org/https://doi.org/10.1016/j.gca.2011.09.019, 2011.

470   Lehner, F. K.: A model for intergranular pressure solution in open systems, Tectonophysics, 245, 153–170, https://doi.org/https://doi.org/10.1016/0040-1951(94)00232-X, 1995.

Macente, A.: 4-dimensional studies of fluid-rock interactions, Ph.D. thesis, School of Geosciences, University of Edinburgh, 2017.

Macente, A., Fusseis, F., Butler, I. B., Tudisco, E., Hall, S. A., and Andò, E.: 4D porosity evolution during pressure-solution of NaCl in the presence of phyllosilicates, EPSL, 502, 115–125, https://doi.org/https://doi.org/10.1016/j.epsl.2018.08.032, 2018.

475   McClay, K.: Pressure solution and Coble creep in rocks and minerals: a review, J Geol Soc London, 134, 57–70, https://doi.org/https://doi.org/10.1144/gsjgs.134.1.0057, 1977.

Merino, E., Ortoleva, P., and Strickholm, P.: Generation of evenly-spaced pressure-solution seams during (late) diagenesis: A kinetic theory, Contrib. to Mineral. Petrol., 82, 360–370, https://doi.org/https://doi.org/10.1007/BF00399713, 1983.

Mimran, Y.: Chalk deformation and large-scale migration of calcium carbonate, Sedimentology, 24, 333–360,
480   https://doi.org/https://doi.org/10.1111/j.1365-3091.1977.tb00127.x, 1977.

Object Research Systems (ORS) Inc, Montreal, C. .: Dragonfly, http://www.theobjects.com/dragonfly.

Paterson, M.: Nonhydrostatic thermodynamics and its geologic applications, Rev. Geophys., 11, 355–389, https://doi.org/https://doi.org/10.1029/RG011i002p00355, 1973.

Peach, C.: Influence of deformation on the fluid transport properties of salt rocks, Ph.D. thesis, Faculteit Aardwetenschappen der Rijksuni-
485   versiteit te Utrecht, 1991.

Peach, C. J. and Spiers, C. J.: Influence of crystal plastic deformation on dilatancy and permeability development in synthetic salt rock, Tectonophysics, 256, 101 – 128, https://doi.org/https://doi.org/10.1016/0040-1951(95)00170-0, 1996.

Peng, T., Thorn, K., Schroeder, T., Wang, L., Theis, F. J., Marr, C., and Navab, N.: A BaSiC tool for background and shading correction of optical microscopy images, Nat Commun, 8, 14 836, https://doi.org/https://doi.org/10.1038/ncomms14836, 2017.

490   Powers, D. W., Lambert, S. J., Shaffer, S., Hill, L., and Weart, W.: Geological Characterization Report, Waste Isolation Pilot Plant (WIPP) Site, Southeastern New Mexico, Tech. rep., Sandia Labs., Albuquerque, NM (USA), https://doi.org/https://doi.org/10.2172/6441454, 1978.

Raj, R.: Creep in polycrystalline aggregates by matter transport through a liquid phase, J. Geophys. Res. Solid Earth, 87, 4731–4739, https://doi.org/https://doi.org/10.1029/JB087iB06p04731, 1982.

Renard, F., Dysthe, D., Feder, J., Bjørlykke, K., and Jamtveit, B.: Enhanced pressure solution creep rates induced by clay particles: Experi-
495   mental evidence in salt aggregates, Geophys. Res. Lett., 28, 1295–1298, https://doi.org/https://doi.org/10.1029/2000GL012394, 2001.

Renard, F., Bernard, D., Thibault, X., and Boller, E.: Synchrotron 3D microtomography of halite aggregates during experimental pressure solution creep and evolution of the permeability, Geophys. Res. Lett., 31, https://doi.org/https://doi.org/10.1029/2004GL019605, 2004.

Rutter, E.: Pressure solution in nature, theory and experiment, J. Geol. Soc. London, 140, 725–740, https://doi.org/https://doi.org/10.1144/gsjgs.140.5.0725, 1983.

500 Rutter, E. and Wanten, P.: Experimental study of the compaction of phyllosilicate-bearing sand at elevated temperature and with controlled pore water pressure, J. Sediment. Res., 70, 107–116, https://doi.org/https://doi.org/10.1306/2DC40902-0E47-11D7-8643000102C1865D, 2000.

Schindelin, J., Arganda-Carreras, I., Frise, E., Kaynig, V., Longair, M., Pietzsch, T., Preibisch, S., Rueden, C., Saalfeld, S., Schmid, B., et al.: Fiji: an open-source platform for biological-image analysis, Nat methods, 9, 676, https://doi.org/https://doi.org/10.1038/nmeth.2019, 2012.

505 Schutjens, P. and Spiers, C. J.: Intergranular Pressure Solution in Nacl: Grain-To-Grain Contact Experiments under the Optical Microscope, in: Dossier: Euroconference on Pore Pressure, Scale Effect and the Deformation of Rocks, 16-20 Nov. 1998, Aussois, France, vol. 54, Oil Gas Science and Technology - Rev. IFP, https://doi.org/https://doi.org/10.2516/ogst:1999062, 1999.

Spiers, C. J. and Schutjens, P. M.: Densification of crystalline aggregates by fluid-phase diffusional creep, in: Deformation processes in minerals, ceramics and rocks, vol. 1, pp. 334–353, Springer, Dordrecht, https://doi.org/https://doi.org/10.1007/978-94-011-6827-4_13, 510 1990.

Stamati, O., Andò, E., Roubin, E., Cailletaud, R., Wiebicke, M., Pinzon, G., Couture, C., Hurley, R. C., Caulk, R., Caillerie, D., et al.: spam: Software for Practical Analysis of Materials, J. Open Source Softw., 5, 2286, https://doi.org/https://doi.org/10.21105/joss.02286, 2020.

Tada, R. and Siever, R.: Pressure solution during diagenesis, Annu. Rev. Earth Planet. Sci., 17, 89–118, https://doi.org/https://doi.org/10.1146/annurev.ea.17.050189.000513, 1989.

515 Thomson, A.: Pressure Solution and Porosity, in: Silica in Sediments, vol. 7, SEPM Society for Sedimentary Geology, https://doi.org/https://doi.org/10.2110/pec.59.01.0092, 1959.

Trurnit, P.: Pressure solution phenomena in detrital rocks, Sediment. Geol., 2, 89 – 114, https://doi.org/https://doi.org/10.1016/0037-0738(68)90030-4, 1968.

Tudisco, E., Andò, E., Cailletaud, R., and Hall, S. A.: TomoWarp2: A local digital volume correlation code, SoftwareX, 6, 267 – 270, 520 https://doi.org/https://doi.org/10.1016/j.softx.2017.10.002, 2017.

Walderhaug, O., Bjørkum, P. A., and Aase, N. E.: Kaolin-coating of stylolites, effect on quartz cementation and general implications for dissolution at mineral interfaces, J. Sediment. Res., 76, 234–243, https://doi.org/https://doi.org/10.2110/jsr.2006.015, 2006.

Weyl, P. K.: Pressure solution and the force of crystallization: a phenomenological theory, J Geophys Res, 64, 2001–2025, https://doi.org/https://doi.org/10.1029/JZ064i011p02001, 1959.

525 Zartman, R. E.: A Geochronologie Study of the Lone Grove Pluton from the Llano Uplift, Texas1, J Petrol, 5, 359–409, https://doi.org/https://doi.org/10.1093/petrology/5.3.359, 1964.

Zimmermann, N. E. R., Vorselaars, B., Quigley, D., and Peters, B.: Nucleation of NaCl from Aqueous Solution: Critical Sizes, Ion-Attachment Kinetics, and Rates, J. Am. Chem. Soc., 137, 13 352–13 361, https://doi.org/https://doi.org/10.1021/jacs.5b08098, 2015.